Substrate Integrated Waveguide Based Millimeter Wave Antennas

Dhruva Kumar Chandrappa

A Thesis
In the Department
of
Electrical and Computer Engineering

Presented in Partial Fulfillment of the Requirements
For the Degree of
Master of Applied Science (Electrical and Computer Engineering) at
Concordia University
Montreal, Quebec, Canada

October 2019

CONCORDIA UNIVERSITY
School of Graduate Studies

This is to certify that the thesis prepared

By: Dhruva Kumar Chandrappa

Entitled: Substrate Integrated Waveguide Based Millimeter Wave Antennas

and submitted in partial fulfillment of the requirements for the degree of

Master of Applied Science (Electrical and Computer Engineering)

complies with the regulations of the University and meets the accepted standards with respect to originality and quality.

Signed by the final examining committee:

_____ Chair and Examiner
Dr. Robert Paknys

_____ External to Program
Dr. Alexey Kokotov

_____ Thesis Supervisor
Dr. Abdel Razik Sebak

Approved By: _____
Dr. Rastko Selmic, Graduate Program Director

November 6, 2019   _____
Dr. Amir Asif, Dean
Gina Cody School of Engineering and Computer Science

Abstract

Substrate Integrated Waveguide Based Millimeter Wave Antennas
Dhruva Kumar Chandrappa
Concordia University, October 2019

Antennas those operating at millimeter-wave (mm-wave) frequencies (30 - 300 GHz) are more advantageous than operating at less than 6 GHz, due to a reduction in antenna physical dimensions, an increase in the data transfer rate, and reduction in latency. However, the electromagnetic waves propagating in free-space at mm-wave frequencies experience significant propagation path loss due to the atmospheric absorption and rain attenuation. Therefore, high-gain antennas are preferred to compensate for path loss and to increase the range of wireless communication. Also, transmission lines such as microstrip, and coplanar waveguides incur high radiation losses at mm-wave frequencies. Hence, to minimize losses, a planar waveguide known as a substrate integrated waveguide (SIW) is preferred. Besides, at mm-wave frequencies, circularly polarized (CP) waves are preferred over linearly polarized (LP) waves as these waves reduce multi-path effects at the receiver.

The objectives of this thesis are to design high-gain linearly, and circularly polarized antennas based on SIW at the mm-wave frequency 30 GHz. The proposed antenna models were designed, simulated, and analyzed using CST software. The antenna prototypes were fabricated and measured for the reflection coefficient, gain, and principal plane radiation patterns. In this thesis, we are proposing two single element antennas, a linear to circular wave polarizer, and an array antenna.

At first, we present, a planar, cylindrical sector-substrate integrated waveguide (CS-SIW) narrow slot antenna. The impedance bandwidth of this antenna is 10.87% which is approximately equivalent to 4 GHz of bandwidth at 30 GHz, and the antenna gain ranges from 8.33 to 8.84 dB within the impedance bandwidth. Further, to improve the gain, an engineered substrate is constructed on top of the CS-SIW slot antenna. The impedance bandwidth of the modified antenna is 10.42% - also, the gain ranges from 10.5 to 11.44 dB over the impedance bandwidth, which implies an increase in the gain from 2.1 to 2.7 dB when compared with the gain of CS-SIW slot antenna. Also, we propose a three-layered meander-line polarizer at 30 GHz which transforms linearly polarized waves to circularly polarized waves for the CS-SIW slot antenna.

Lastly, we present, a 1×8 CS-SIW slot antenna array with a superstrate to achieve a high-gain LP antenna. The impedance bandwidth of the antenna is 10%. The gain of the array antenna integrated with a superstrate layer varies from 21.35 to 22.95 dB over the impedance bandwidth.

Acknowledgments

I would like to express my sincere gratitude to my advisor Dr. Abdel Razik Sebak for the continuous support and encouragement throughout the MASc. program. I would also like to thank both the committee members Dr. Robert Paknys and Dr. Alexey Kokotov for reviewing the manuscript, and their valuable feedback.

Also, I would like to thank Mr. Traian Antonescu (Polytechnique Montreal University) for fabricating all the antenna prototypes mentioned in this document. And, Mr. Maxime Thibault (Polytechnique Montreal University) and Mr. Vincent Mooney-Chopin (Concordia University) for their help on antenna radiation pattern measurements.

I would like to extend my thanks to all my beloved friends and colleagues namely (in no particular order): Ali, Nadeem, Shraman, Sifat, and Yazan — for all our (non) technical discussions, and for making the workplace lively and memorable.

Lastly, but not the least, I would like to take this opportunity to thank my family wholeheartedly for all their unconditional love and support.

To my parents, Chandrappa and Lalitha, and sister, Bhavya.

Table of Contents

List of Figures

xii

List of Abbreviations

AMC   artifical magnetic conductor

CP   circular polarization

CS-SIW   cylindrical sector substrate integrated waveguide

CST   Computer Simulation Technology

DTR   data transfer rate

EBG   electromagnetic bandgap

EM   electromagnetic

FTBR   front to back ratio

GCPW   grounded coplanar waveguide

LHCP   left-hand circular polarization

LNA   low noise amplifier

LOS   line of sight

LP   linear polarization

mm-wave   millimeter-wave

NLOS   non-line of sight

PA   power amplifier

PCB   printed circuit board

PMC   perfect magnetic conductor

RHCP   right-hand circular polarization

Rx   receiver

SIR	signal to interference ratio
SIW	substrate integrated waveguide
SLL	side lobe level
TE	transverse electric
TEM	transverse electromagnetic
TM	transverse magnetic
Tx	transmitter
UE	user equipment
UHF	ultra high frequency
VNA	vector network analyzer
WLAN	wireless local area network
WPAN	wireless personal area network
WR	rectangular waveguide

Chapter 1: Introduction

Wireless communication has seen tremendous growth in the modern world. Therefore, wireless application ranges from defense to medical industries (see [1], p.116). An antenna is a backbone for the existence of any wireless communication. Antennas are designed, tuned to operate at the dedicated frequency (which imply, a wireless device operates at that frequency), and their properties differ from application to application. Each wireless device consists of an antenna; to transmit (or receive) electromagnetic (EM) waves to (or from) free-space (see [2], p.1-4). The radiated EM waves carry information while propagating in free-space and thus enabling wireless communication link between transmitter and receiver.

The most popular wireless networks are a cellular network, wireless local area network (WLAN), and wireless personal area network (WPAN). Due to a large number of users often use user equipment (UE) devices to transmit and receive information, as shown in figure 1.1. UE devices, to name a few, are cellular phones, tablets, smart-watch. As the number of UE devices per person increases, the number of links has to be interlinked with the access points such as Wi-Fi, for wireless communication to be successful. Scaling the above scenario to thousands of users leads to a myriad of wireless links, e.g., at densely populated areas. At this instance - users experience high latency, decrease in service quality, and unstable wireless connectivity.

Increasing channel bandwidths can solve the above challenges for each wireless application (see [3], p.14). However, for frequencies less than 6 GHz, the frequency spectrum is overcrowded by a diversity of wireless applications, which mean, wide channel bandwidths are unfeasible (see [3], p.3), [4].

The search for the availability of wide channel bandwidths is scanned across the frequency spectrum and found at millimeter-wave (mm-wave) frequencies. The mm-wave frequency ranges from 30 - 300 GHz, and the corresponding free-space wavelength, $\lambda_0 = c/f$, is between 10 - 1 mm, respectively (where c is the speed of light and is $\simeq 3 \times 10^8$ m/s). Currently, the only applications operating at mm-wave are military and radar. Hence, most of the mm-wave frequency spectrum is unused, and wide bandwidths are feasible. For instance, 1 GHz of bandwidth is readily available at frequencies 28 GHz and 38 GHz (see [3], p.5).
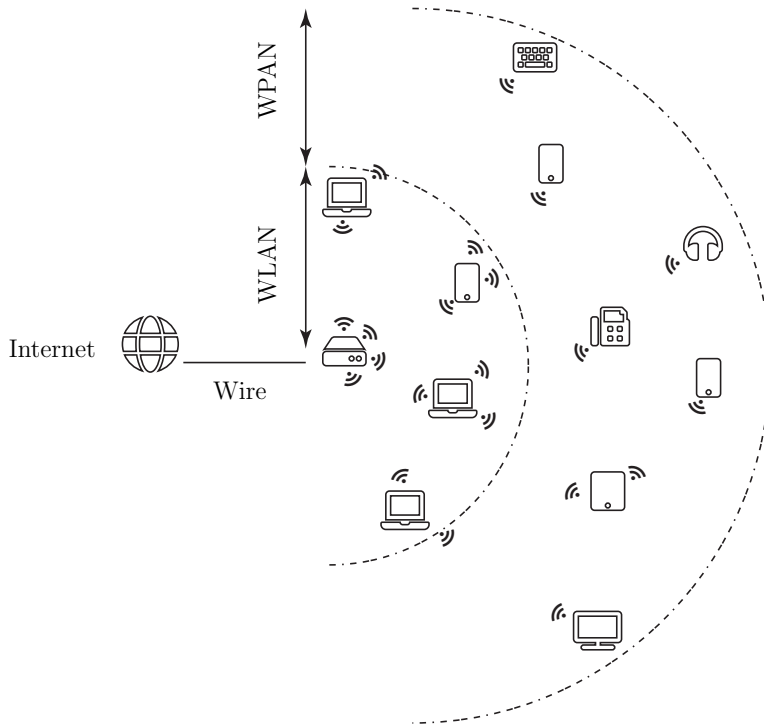
Figure 1.1: Representation of WLAN and WPAN for indoor environment. The coverage area for WLAN is between 10 - 100 m, and WPAN is < 10 m (see [3], fig. 1.7, 1.9).

At mm-wave frequencies, the EM wave propagating in free space experience path loss due to atmospheric absorption and rain attenuation as free space wavelengths are shorter in the order of millimeters. The plot of atmospheric absorption loss (in dB/km) and rain attenuation (dB/km) for multiple rain velocity versus frequency (in GHz) are shown in figure 1.2(a) and 1.2(b). As read from figure 1.2, the combined atmosphere and rain attenuation losses (assuming high rain velocity) increases as frequency increases. Therefore, the long-range wireless communication system is not suitable at mm-wave frequencies.

However, to overcome the propagation path loss, two solutions can be employed: (a) to reduce the distance between the transmitter and receiver to about less than 200 m [4, 5]. For instance, at 28 GHz, the atmospheric absorption is equal to 0.012 dB, and the rain attenuation is equal to 1.4 dB for hefty rainfall (of 25 mm/hr). Therefore, the number of base stations supporting cellular networks increases drastically from today's base stations, which are operating below 6 GHz. (b) to design and build a high gain antenna system that can overcome the barrier of propagation path loss and still would be sufficient to cover long-range distances.
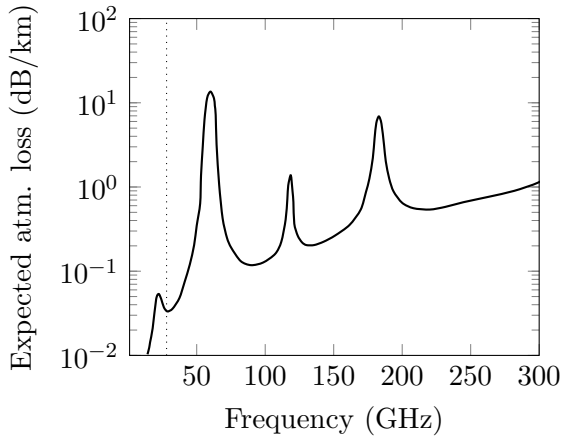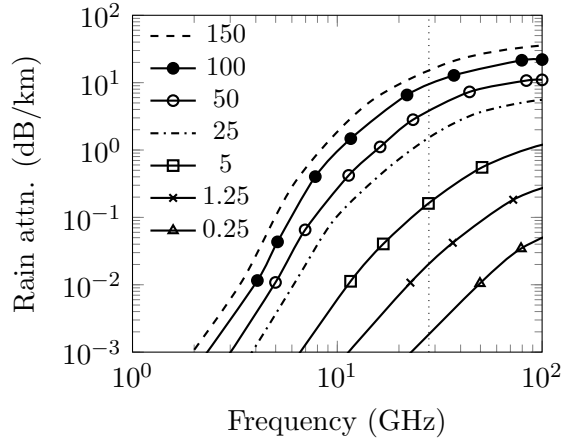
Figure 1.2: (a) Plot of expected atmospheric absorption loss (in dB/km) versus frequency (in GHz) [5]. (b) Plot of rain attenuation (in dB/km) versus frequency (in GHz) at multiple rain velocities (in mm/hr) [5].

1.1 Motivation and Problem Statement

At mm-wave frequencies, free-space propagation path loss dominates (see [3], pg.100). Therefore, to overcome path loss, a high-gain (directional) antennas must be employed to communicate over a long distance. In general, for an antenna to radiate efficiently - the antenna size should be comparable to its operating wavelength, for example, a resonant dipole antenna. By taking advantage of this fact, an antenna operating at mm-wave frequency occupies small area (thus, less resource) when compared to antennas operating at UHF or below (more resource).

At mm-wave frequencies and beyond, unbounded transmission lines such as microstrip, coplanar waveguide, exhibit high radiation losses; and has low power handling capability. Therefore, to overcome these challenges, a planar waveguide such as a substrate integrated waveguide (SIW) is preferred.

At mm-wave frequencies, linearly polarized waves are susceptible to multi-path due to a reflective materials readily available in the environment [4]. Multi-path is observed at the receiver when a line of sight (LOS) signal and non-line of sight (NLOS) signal arrive at the same time with different phases. Thus, when an antenna radiates linearly polarized waves there are higher chances that the phase of the LOS and NLOS signals are out of phase with

3

each other. Therefore, the receiver must be able to use all the resources to identify and process the signal. However, by using a circularly polarized antenna, multi-path effects can be reduced (see [1], p.120).

1.2   Objectives

High-gain antennas overcome the difficulties mentioned in section 1.1. The main objective of this thesis is to design high-gain linearly, and circularly polarized antennas based on SIW at 30 GHz and includes the following two main tasks:

1. To design, simulate, fabricate, and measure a low-profile planar antenna element at the center frequency, f_c, equal to 30 GHz. Also, to design a wideband standalone polarizer which can transform linearly polarized waves radiating from an antenna to circularly polarized waves at f_c.

2. To design design, simulate, fabricate, and measure a high gain antenna array system at f_c.

1.3   Theoretical Background and Design Methodology

The purpose of an antenna is to send and receive EM waves. However, these waves are both direction and polarization dependent which are spatially distributed over a spherical coordinate system surrounding the antenna. As a result, to understand visually, we can sketch the principal E plane and H plane radiation patterns of an antenna on a 2D polar plot. These principal patterns depend on the distribution of time-varying currents on the antenna physical aperture. Therefore, the calculation for the total current distribution on the antenna aperture is imperative. Not all antenna apertures are as simple as a resonant dipole antenna. Therefore, rigorous and complex numerically methods should be incorporated for complex apertures in order to calculate currents. Some of the numerical methods to name a few are FDTD (Finite-Difference Time-Domain), FEM (Finite Element Method), MoM (Method of Moments) (see [1], Chap 14).

Material selection
(relative permittivity and thickness of a dielectric substrate)

↓

Antenna modelling using CST-MS software
(geometry, radiating element, feeding structure)

↓

Define port, and boundary conditions (if any)

↓

Full wave analysis by choosing a suitable solver and optimization
(transient solver, eigenmode solver)

↓

Antenna fabrication

↓

Fabricated antenna measurements
(VNA, anechoic chamber)

Figure 1.3: Flowchart of antenna design methodology.

Design Methodology

The antenna design methodology involves the selection of a suitable dielectric substrate to fabricate SIW structures. Furthermore, the substrate thickness and relative permittivity are crucial for designing an antenna. The model of an antenna is constructed using commercial software such as CST, followed by defining the port and boundary conditions. The port acts as a signal source for an antenna. The full-wave analysis of the designed antenna model is carried out by choosing the appropriate solver such as time-domain or frequency-domain solver. The eigen mode solver perform the analysis of periodic structures in CST. The CST utilizes FDTD numerical technique to obtain a solution to the designed model. The results of a solution, to name a few are reflection coefficient, radiation patterns, gain estimation, efficiency. Further, if necessary, the model parameters are optimized to achieve satisfactory results.

Next, to validate the simulated results obtained from CST, the prototype of the antenna

model is fabricated and measured. The reflection coefficient of the antenna model is measured using a vector network analyzer, while the antenna radiation patterns are measured using an anechoic chamber. Figure 1.3 depicts the design methodology flowchart. In this flowchart, most of the steps remain unchanged for various antenna problems except the antenna modeling (i.e., step 2).

1.4   Thesis Outline

Chapter 2 covers the literature survey. We begin with the theoretical understanding of the slot antenna and introduce the concept of complementary antennas. Also, it includes design, theory, and analysis of the SIW structure. In Chapter 3, we propose three single element antennas at 30 GHz. These antennas radiate LP waves. Also, by designing a meander-line polarizer, the transformation of LP waves to CP waves is shown. In Chapter 4, we present a high-gain antenna array system by designing a SIW corporate feeding network. At last, in Chapter 5, we conclude the thesis with a summary and discuss the feasibility of extending this work in the future.

Chapter 2: Background

2.1 Introduction

Planar antennas (such as slot or patch antenna) are low-profile, light-weight, and low-cost antennas. These antennas can be easily integrated with the other RF components (such as amplifiers, filters, switches) on a printed circuit board (PCB) to build a transceiver. As a result, planar antennas are preferred in various applications, to name a few, aircraft, spacecraft, satellite, cellular phones - owing to their low-profile nature (see [6], chap.12 and 14). Therefore, in this thesis, our dedication was inclined towards slot antenna based on substrate integrated waveguide (SIW) technology.

In this chapter, we begin with a discussion on the theoretical analysis of slot antennas. It is followed by an explanation of complementary structures and usefulness of Babinet's Principle. Later, planar form of dielectric rectangular waveguide known as substrate integrated waveguide (SIW) is discussed. Also, we shall present a few existing SIW slot antennas available in the literature.

2.2 Slot Antenna

The slot antenna belongs to a family of aperture antennas. Aperture antennas are antennas in which the EM waves radiate from the aperture or an opening. A few other examples for aperture antenna include horn, lens, reflector, and surface-wave antennas. A slot antenna is the simplest of all aperture antennas to design and construct. And, is realized by etching a slot on an infinite conductor such as aluminum or copper as shown in figure 2.1. Since aircraft's and spacecraft's outer body is a conductor, slot antennas can be flush-mounted on the conductor surface and are thus preferred for space applications.

Let us now assume that the infinitely extending infinitesimal thickness conductor (including slot) is dividing the whole region into two halves at the origin as shown in figure 2.1. Let, $z < 0$ denote medium-1 consisting of air. Similarly, $z > 0$ denotes medium-2
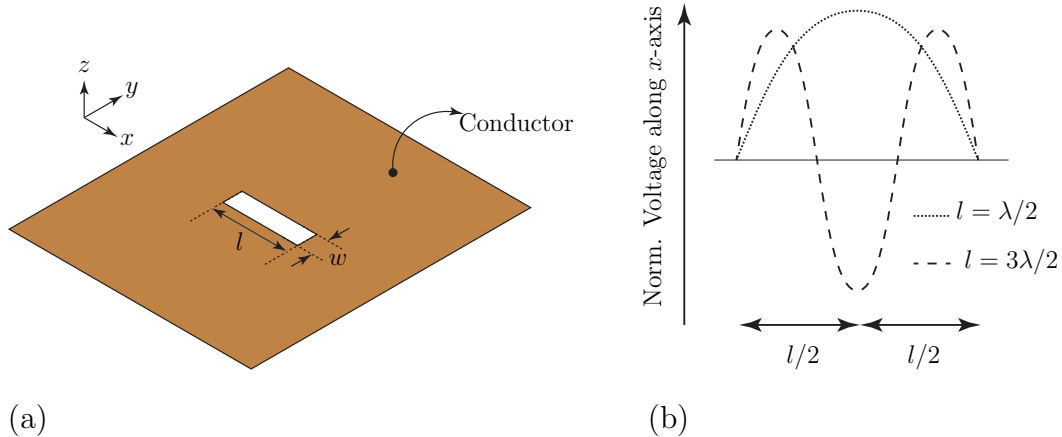
Figure 2.1: (a) A slot on an infinite conductor sheet. (b) Illustration of the normalized voltage distribution inside the slot for slot lengths, l, equal to $\lambda/2$ and $3\lambda/2$.

which is source-free and consisting of air. For an EM wave traveling from medium-1 towards medium-2, it has to pass via slot with dimensions $l \times w$. The infinite conductor acts as a short circuit (barrier) and thus won't let any field to penetrate through it. Therefore, the size and the shape of the slot on the conductor determines the quantity of field in medium-2. For instance, if we cover the slot area by using a conductor, no wave can propagate to medium-2 (field-free behavior still exists). Further extending the above concept to slot as an antenna, the shape and size of the aperture or slot are frequency-dependent quantities that help to determine the center frequency, input impedance and polarization of the EM field in medium-2.

To understand the behavior of a slot antenna in terms of voltage and current, let us connect an AC signal source to the slot narrow wall along the y axis at position $l/2$ shown in figure 2.1(a). We also assume that the slot length, l, is equal to $\lambda_0/2$ and slot width, w, is $w \ll \lambda_0$. The analogy is similar to the transmission line terminated with short circuit load at distance $\lambda_0/4$ from the source. We can now solve this problem by using transmission line analysis inside the slot. We can calculate that, the voltage is maximum at the center of the slot, and minimum at the ends of the slot as shown in 2.1(b) for $l = \lambda_0/2$. However, the current is minimum at the center of the slot, and maximum at the ends of the slot. In addition, the currents are out of phase at the ends of the slot along the x axis. When the impedance of the AC source is matched with the impedance of slot antenna at resonance, the slot antenna radiates EM field on either side of the conductor (i.e., $+z$ and $-z$ axis) due to the in phase distribution of the voltage along the x axis.

To determine the specific radiated fields from the slot antenna, we need to know the value of surface current distribution on the conductor. For instance, for wire antennas (such as dipole antenna) the impressed current density, **J**, exists only on the wire. We can calculate vector potential, **A**, using **J**. The magnetic field, **H**, can be calculated using **A** and subsequently, **E**, from **H** using Maxwell's curl equation (see [7], sec 4.1). We can follow a similar procedure for slot or aperture antennas to calculate the radiated fields by knowing the surface current. When the AC signal is applied to the slot as shown in figure 2.1, the impressed currents travel across the conductor and won't refrain well within the slot. However, if the conductor extends over infinite distances, we can make use of image theory for simplification [1]. However, infinite structures are not realizable. Another approach is to evaluate the field over the slot alone, rather than considering the abundance of a conductor. The curling electric fields are replaced with magnetic current density, **M**, along the length of the slot. If the specific fields were known at every point on the face of the slot, we can calculate radiated fields from the slot.

2.3   Complementary Antennas: Babinet's Principle

Consider a slot antenna, as shown in figure 2.1. If we were to replace the conductor with air and fill the slot with a conductor, we would achieve slot antennas dual structure. In this case, it is a dipole antenna. Thus, both slot and dipole antennas are said to be complementary antennas, as shown in figure 2.2. In 1946, Booker derived an equation between the impedance of the slot and dipole antenna considering polarization using Babinet's principle [8] (see [6], sec 12.8).

Since dipole antennas are easily understood and analyzed, using Babinet's principle, we can readily calculate the impedance of the slot antenna. If Z_{slot} is the impedance of the slot antenna and Z_{dipole} is the impedance of the dipole antenna, then by Babinet's principle:

$$Z_{slot}Z_{dipole} = \frac{\eta^2}{4} \tag{2.1}$$

Where η is the intrinsic impedance of the ambient medium of complementary antennas. If air is the ambient medium, $\eta = \eta_0 = 377 \ \Omega$

Further, Babinet's principle tells us if the radiation pattern of an antenna is known, the radiation pattern for its dual antenna can be obtained by interchanging principal E plane

9
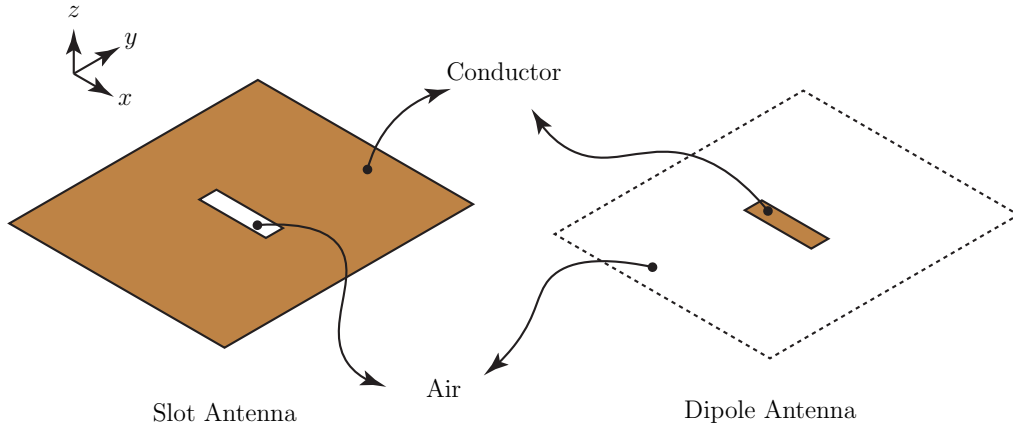
Figure 2.2: A slot antenna and its complementary structure, a dipole antenna. Air is replaced with conductor, and conductor is replaced with air to obtain complementary antenna.
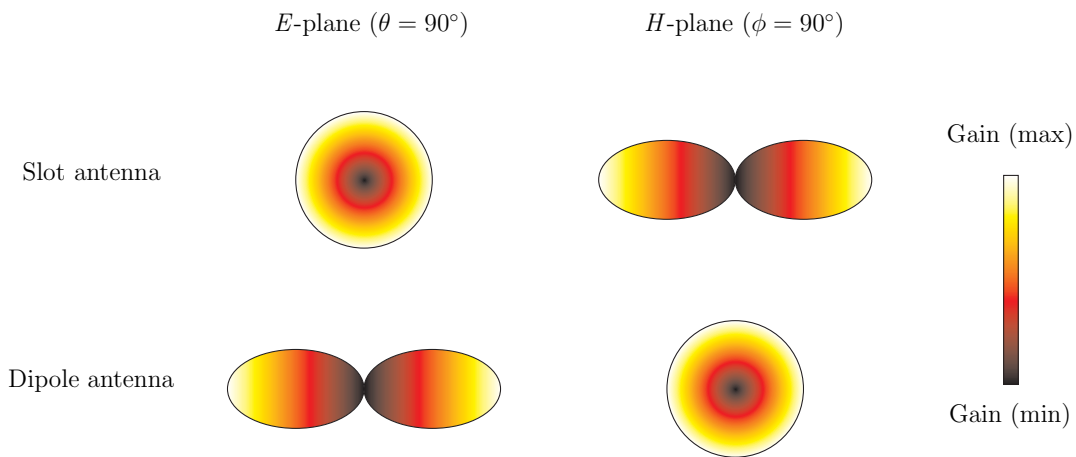
Figure 2.3: Principal E and H radiation patterns for the slot and dipole antenna oriented along x axis.

and H plane radiation patterns. Therefore, for an x-directed dipole and slot antenna shown in figure 2.2, we can plot the principal E plane and H plane radiation patterns as illustrated in figure 2.3.

2.4   Substrate Integrated Waveguide (SIW)

A waveguide is a 3-D structure which guides an EM wave from one point to another. A waveguide can be hollow or filled with a dielectric substrate bounded by a conductor. The EM wave travels along the waveguide's longitudinal axis in a zig-zag path. The radiation loss
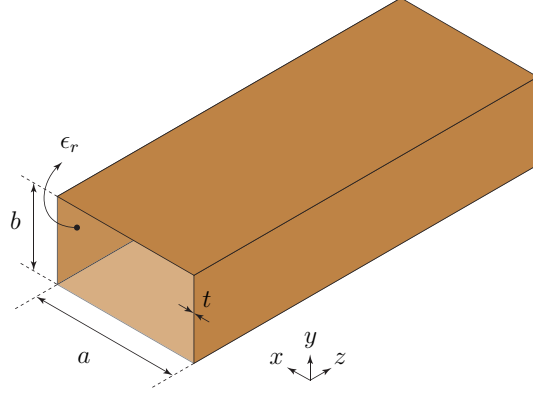
Figure 2.4: 3D model of rectangular waveguide.

for the wave propagating inside the waveguide is zero. Because when the wave interacts with the air-conductor interface, the wave reflects inside the waveguide; enforcing air-conductor boundary conditions assuming the conductor thickness is much larger than the skin depth. In addition, the attenuation loss in a waveguide is frequency-dependent and increases as the frequency increases. For example, for the rectangular waveguide (WR) operating in TE_{10} mode and constructed with copper, the losses using (see [9], eq. 3.96) are 0.576 dB/m for WR-28 at 32 GHz, and 1.51 dB/m for WR-15 at 60 GHz.

Waveguides can take many shapes due to their 3-D structure. To differentiate between several waveguides, we can prefix the waveguide depending on the shape of the waveguide cross-section. Thus, the rectangular waveguide has a cross-section in the shape of a rectangle. Likewise, the circular waveguide has a circular cross-section and so on. The 3-D model of the hollow ($\epsilon_r = 1$) rectangular waveguide with conductor thickness, t, is shown in figure 2.4. The waveguide cross-section is in the xy plane, and the dimensions are a and b (where $a > b$) along x and y, respectively. Also, the waveguide longitudinal (or wave propagation direction) is along the z axis. In general, a waveguide supports transverse electric (TE) or transverse magnetic (TM) waves. However, the propagation of a transverse electromagnetic (TEM) wave is not possible inside the waveguide due to unsatisfied boundary conditions at the cross-section of the conductor perimeter.

Since we are interested in the planar form of waveguide (such as SIW), the derivation and analysis on the conventional rectangular or circular waveguide is out of scope from this thesis, and one can refer to (see [7], chap.3).

Substrate Integrated Waveguide (SIW)

The excitation of the slot antenna driven by an AC source (figure 2.1) is delicate at the intersection of the source terminals and conductor. Therefore, we have to replace the AC source by introducing a feeding mechanism that can excite the slot and also provide similar behavior as the source. Since we are interested in designing planar antennas, preference is given to planar feeding structure rather than rectangular waveguide, as shown in figure 2.4. Examples of planar feeding structure include, but not limited to, microstrip, stripline, SIW, grounded coplanar waveguide (GCPW). Microstrip feeding structure is one of the famous transmission lines and easy to design. However, the preferred choice of SIW as a feeding structure over microstrip is because of SIW exhibit high-quality factor, power handling, elimination of surface waves, and low attenuation losses as frequency increases at Ka-band. The disadvantages of SIW over microstrip include ease of fabrication, low bandwidth, and exhibit cut-off frequency [10].

The conventional dielectric-filled rectangular waveguide is modeled in the planar form by using a dielectric substrate with copper cladding on both sides and replacing the side walls with a periodic distribution of vias. A via is a metal cylinder that may be either hollow or solid in shape. The vias are inserted to the dielectric substrate, and the via height should be equal to the thickness of the dielectric substrate. Thereby, a via connects both top and bottom copper cladding available on the substrate. The resulting waveguide in the planar form is known as Substrate Integrated Waveguide (SIW). As a result, the SIW fabrication cost is less compared to conventional WR.

The wave propagation constant, field distribution of electric, magnetic and surface currents, cut-off frequency, and the dispersion characteristics of SIW are similar to that dielectric-filled rectangular waveguide as shown in [11]. However, the guided waves along the SIW by exciting only TE_{mn} ($n = 0$) mode (such as TE_{10}, TE_{20}) [11]. Because, the SIW sidewalls (i.e., via) and the longitudinal surface current, $\mathbf{J_s}$, for all the other mode(s) (except TE_{m0}) are orthogonal to each other. This orthogonality behavior implies, SIW as an antenna and a significant amount of energy leaks out from the SIW sidewalls. So thus, these modes are not suitable for guiding waves. The dominant mode of the SIW is TE_{10} mode. The subscript, m, in TE_{m0} represents the number of half-wave variations of the electric field along the SIW width, and m can take any integer from 1 to ∞.

Using the SIW design equations given in [11], the uniform SIW is designed using CST software; and is constructed on Rogers 6002 substrate with $\epsilon_r = 2.94$ backed by a thin
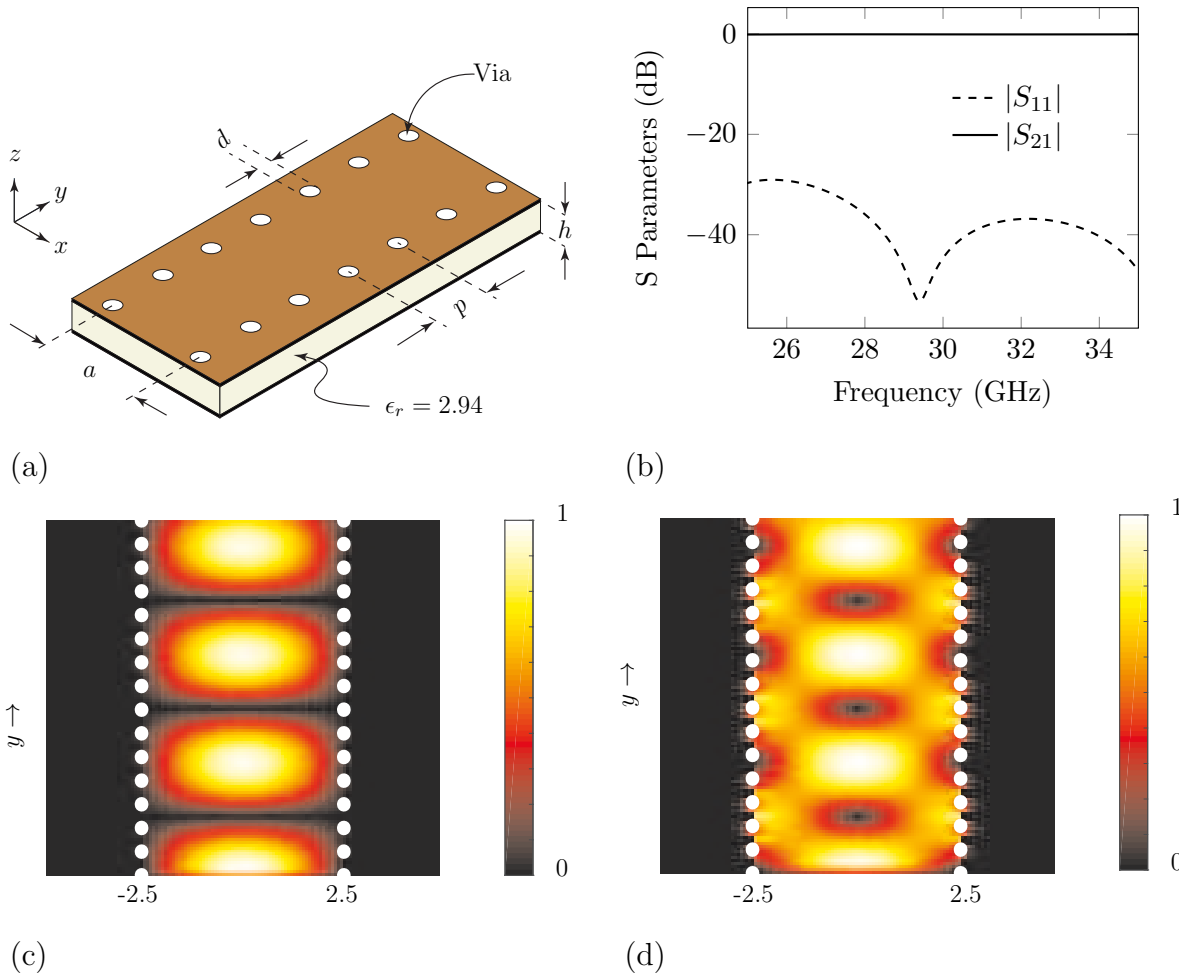
Figure 2.5: (a) 3D model of an uniform SIW and its dimensions are $h = 0.508$, $d = 0.4$, $p = 0.8$ and $a = 5$ (all are in mm); (b) S-parameters of a two-port reciprocal uniform SIW model; (c) Top view of $|\mathbf{E}|$ field (V/m) inside uniform SIW, normal to z; and, (d) Top View of $|\mathbf{H}|$ field (A/m) inside uniform SIW, normal to z.

copper cladding of thickness 17.5μm on both top and bottom sides of the substrate as shown in figure 2.5(a). The SIW is in the xy plane; the two wave-ports are positioned at the end of the SIW and are normal to the y axis. The simulated scattering parameters for the two-port uniform SIW is given in figure 2.5(a). As seen in figure 2.5(b) most of the energy is transferred from port 1 to 2; which is captured by the $|S_{21}|$ parameter, and is less than -0.12 dB across the frequency range 25 - 35 GHz. The distance between the SIW side walls is such that the waveguide operates in the TE_{10} dominant mode. The electric and magnetic field components existing inside the uniform SIW are E_z, H_x, and H_y. The illustration of a contour plot for both electric and magnetic fields at 30 GHz are shown in figures 2.5(c) and 2.5(d) respectively.
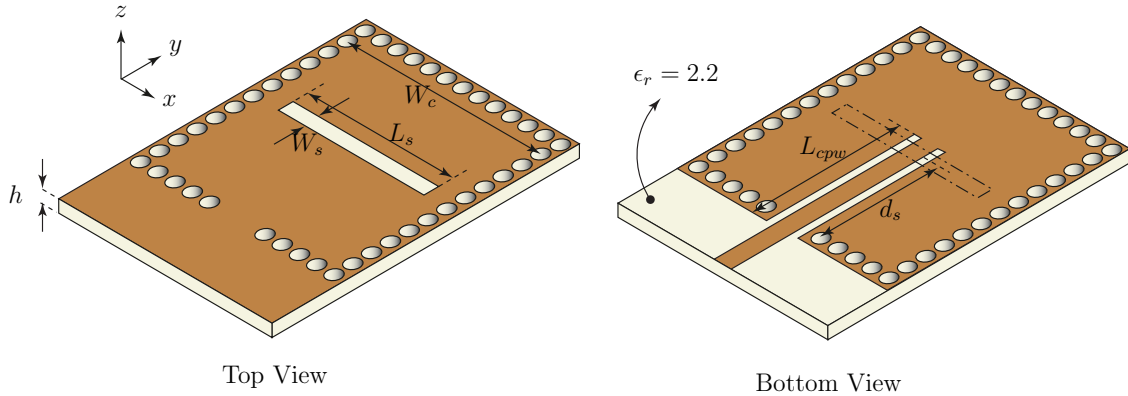
Figure 2.6: SIW cavity backed planar slot antenna (redrawn from [12]).

2.5 SIW based Slot Antennas

2.5.1 Linearly Polarized Antennas

In [12], a low-cost, low-profile planar slot antenna is constructed on a thin Rogers 5880 dielectric substrate using an SIW cavity as shown in figure 2.6. The thickness of the substrate is $\simeq \lambda_0/50$ (where λ_0 is the free space wavelength at 10 GHz). The SIW cavity is excited by constructing a grounded coplanar waveguide (GCPW), and the cavity dimensions are designed to form TE_{120} mode. A slot is etched on the opposite side of the GCPW. The surface currents are maximum and are pointing in the longitudinal direction (along the y-axis). Due to the resonance characteristics of the slot at a single frequency (i.e., at 10 GHz), the impedance bandwidth is found to be 1.7%. The gain and front-to-back ratio (FTBR) are found to be 5.4 dB and 16.1 dB, respectively.

Further, to overcome the narrow impedance bandwidth of the slot antenna [12], two antenna designs are proposed in [13] and [14]. In [13], a bow-tie slot is etched in the place of the narrow slot using the similar concept presented in [12]. Figure 2.7 displays the top and bottom view of the proposed bow-tie slot antenna in [13]. The impedance bandwidth is improved to 9.4% from 1.7% by generating two modes (TE_{110} and TE_{120}) inside the bow-tie slot. The resonances of these modes are at frequencies 9.98 GHz and 10.6 GHz. As reported, a minimum gain of 3.53 dB is achieved over the impedance bandwidth and has an FTBR of 15 dB and 20 dB, at 9.98 GHz and 10.6 GHz, respectively.

In [15], a wide slot is designed on the dielectric substrate of thickness 0.635 mm having
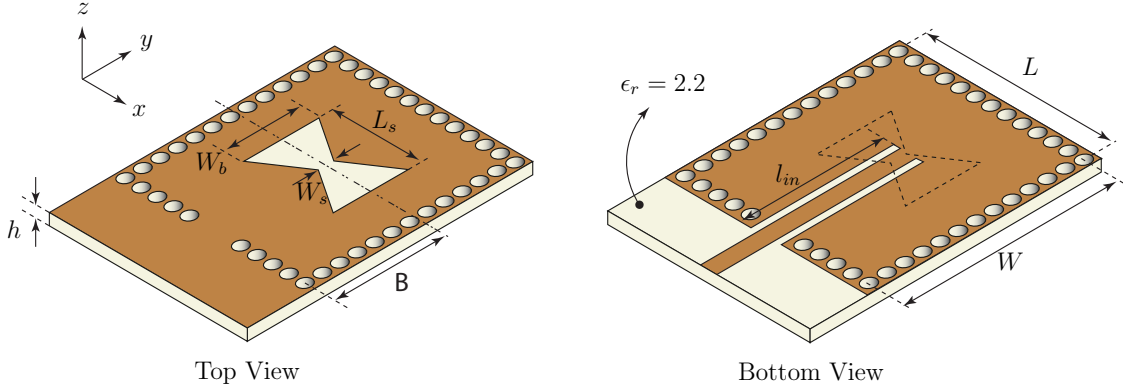
Figure 2.7: SIW cavity backed bow-tie slot antenna (redrawn from [13]).
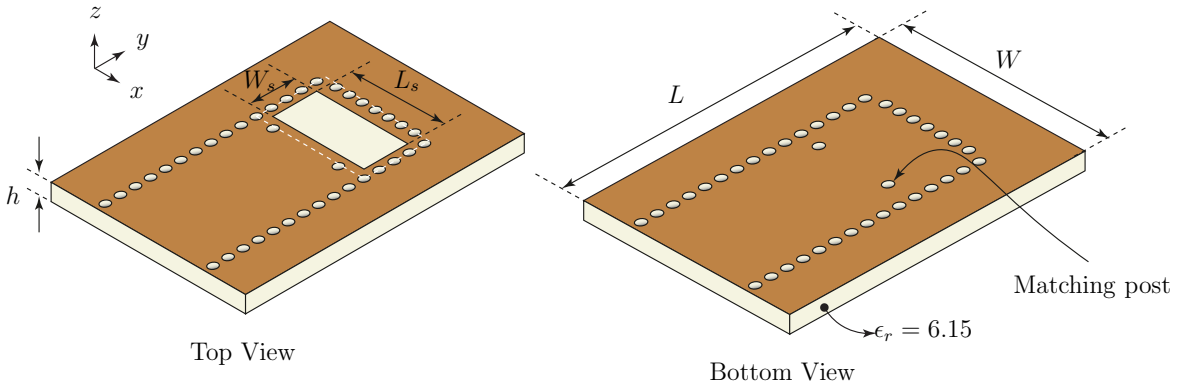
Figure 2.8: SIW cavity backed wide slot antenna (redrawn from [15]).

relative permittivity, $\epsilon_r = 6.15$ at 60 GHz as shown in figure 2.8. A matching post is inserted to the substrate close to the radiating element, which acts as a resonant cavity at 62.8 GHz. A slot with width to length ratio (WLR) = 0.71 produces another resonance at 59.2 GHz. Thus, when these two resonances are close to each other, a wideband impedance bandwidth of about 11.6% is achieved from the range 57 - 64 GHz. The simulated gain at resonant frequencies (59.2 GHz and 62.8 GHz) are 7.4 dB and 7.9 dB, respectively. To further increase the gain, a 2×4 antenna array was constructed, as shown in figure 2.9. The impedance bandwidth of the array was 11.5%, and the measured gain was less than 12 dB for the overall bandwidth. In [16], a planar array antenna consisting of 12×12 radiating elements (slots) was excited by designing a 12-way linear power divider as shown in figure 2.10. The frequency of operation for this antenna array was at 60 GHz. The given impedance bandwidth is about 4.12%, and the maximum gain is 22 dB.

15
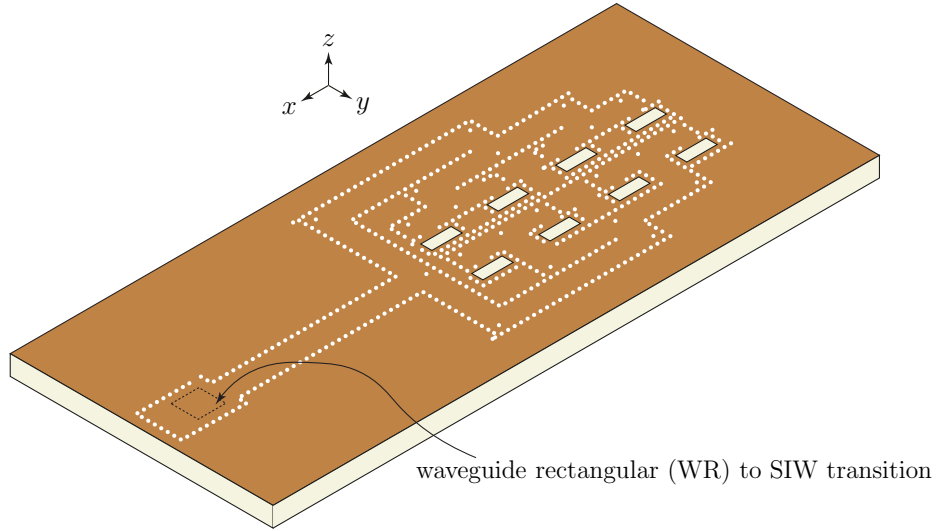
Figure 2.9: A SIW cavity backed wide slot antenna array consisting of 2×4 elements (redrawn from [12]).
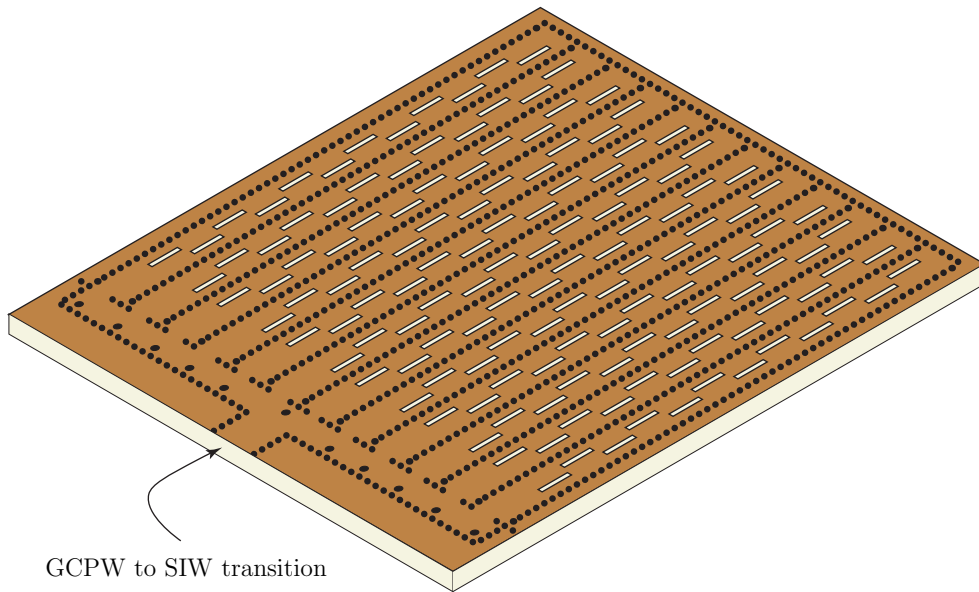
Figure 2.10: High gain planar array antenna designed at 60 GHz (redrawn from [16]).

2.5.2 Circularly Polarized Antennas

A compact circularly polarized (CP) antenna is shown in [17]. The antenna is designed using a Rogers 5880 substrate of thickness, $h = 0.5$ mm $\simeq \lambda_g/40$ (where $\lambda_g = \lambda_0/\sqrt{\epsilon_r}$ is the guided wavelength inside the substrate at 10 GHz). The two radiating narrow slots are
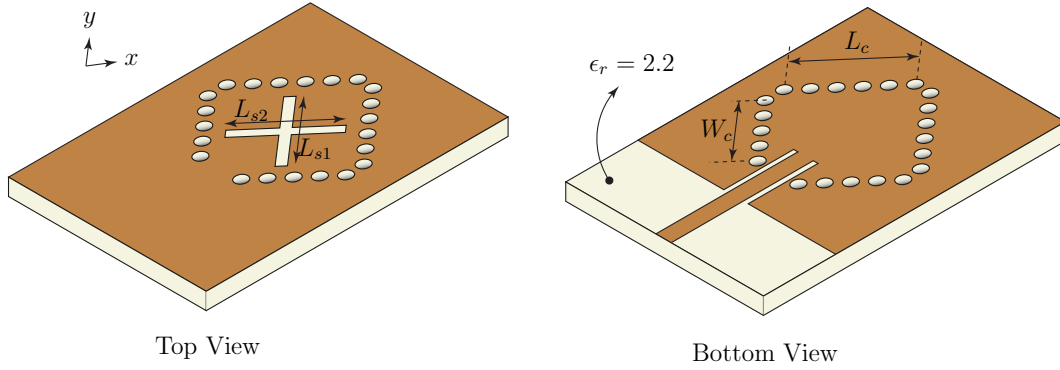
Figure 2.11: SIW cavity backed crossed slot antenna (redrawn from [17]).
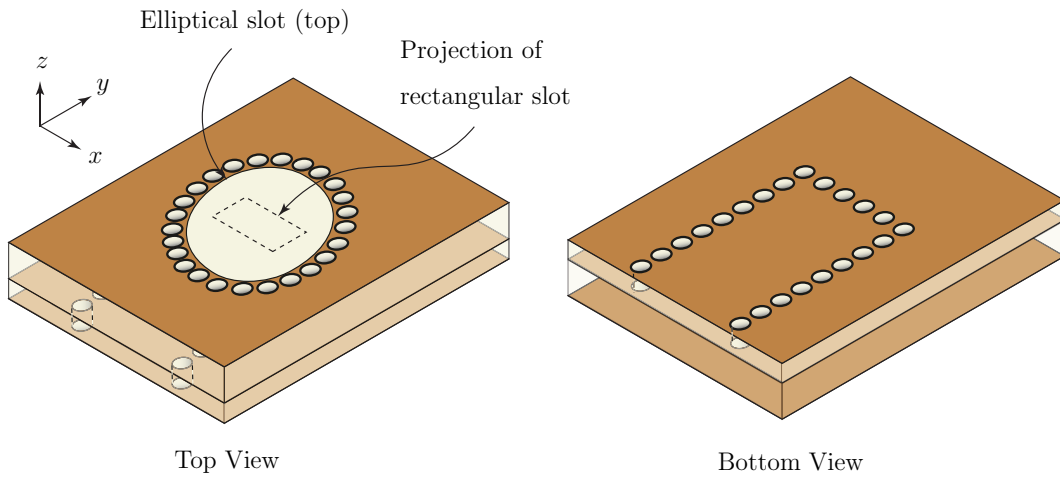
Figure 2.12: Wideband circularly polarized SIW cavity-backed antenna (redrawn from [18]).

etched on top of the SIW cavity fed by GCPW. Also, the slots are rotated by 45° relative to one another, as shown in figure 2.11. The CP from the slot is achieved by establishing two orthogonal modes (TE_{120} and TE_{210}) inside the square SIW cavity. The reported, measured impedance bandwidth and axial ratio (AR) bandwidth for the antenna are 3% and 0.8%, respectively. The gain varies from 6 - 6.15 dB in the impedance bandwidth, and the FTBR is about 29.6 dB.

Further, a multi-layer antenna configuration consisting of two or more substrates was preferred to achieve CP at 24.5 GHz and 60 GHz. In [18], the short-circuited SIW carrying its dominant (TE_{10}) mode was constructed on a thin bottom layer. A rectangular slot is etched on top of the SIW close to the short-circuited wall. On top of the rectangular slot, the elliptical cavity using SIW technology is constructed on a thick dielectric substrate. The elliptical cavity is rotated by 45° relative to the rectangular slot, and an elliptical slot is
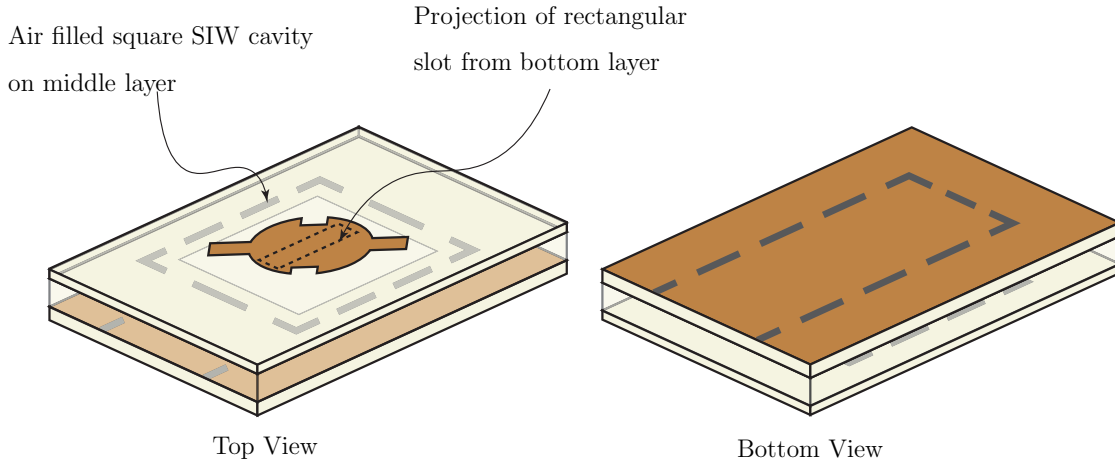
Figure 2.13: Three layered SIW cavity based CP antenna (redrawn from [19]).

constructed on the top metal layer, as shown in figure 2.12. The observed wide impedance bandwidth is about 42.2%. Due to the combined resonance of the slot and the elliptical cavity. The observed, AR bandwidth is 5.6%, and the gain of the antenna varies from 7.6 - 8.7 dB in the impedance bandwidth.

In [19], a longitudinal rectangular slot is constructed on an SIW waveguide to resonate at 60 GHz. Above the slot, a square air-filled SIW cavity is constructed on a thick substrate by removing copper traces on both sides. Above the cavity, a modified circular patch to achieve CP has been etched on a fragile substrate (top layer) as shown in figure 2.13. The AR bandwidth and the impedance bandwidth of the proposed antenna are 6.6% and 11.57%, respectively. The average gain for the impedance bandwidth is 7.8 dBic.

Chapter 3: The Linear and Circular Polarized Cylindrical Sector (CS)-SIW Narrow Slot Antenna

3.1 Introduction

In general, the slot antenna suffers from narrow bandwidth due to its' resonant behavior [12]. To increase the slot antenna bandwidth (>9.5%), a bow-tie slot; a cavity slot antenna on a thick ($\simeq 0.32\lambda_g$) dielectric substrate [15] is presented. However, in this chapter, we are proposing a SIW slot antenna on a thin (0.09 λ_g) substrate which can achieve >10% bandwidth at the center frequency, f_c, 30 GHz.

The methodology for the design of the CS-SIW narrow slot antenna is as follows: the concept and realization of the cylindrical sector SIW from the conventional SIW model. Further, to excite the CS-SIW model, two transitional layers are constructed using microstrip line and SIW. Later, the slot is etched on the top layer of the CS-SIW. The antenna model is designed and simulated using a commercial 3D EM software, Computer Simulation Technology (CST) (version 2017.05) [20]. Parametric analysis was used in CST to study the dimensions and position of the slot.

Further, to validate the simulated results (such as reflection coefficient, $|S_{11}|$, gain, and principal plane radiation patterns) obtained from the CST software. A CS-SIW antenna was fabricated and measured. The antenna reflection coefficient was measured using a vector network analyzer (VNA). Both the gain and the radiation patterns are measured using the anechoic chamber. Finally, a comparison is made between the measured and the simulation results.

In addition, in this chapter, we design a three-layer meander-line polarizer unit cell to transform linear to circular polarized waves using CST software. Also, the polarizer and the CS-SIW slot antenna (acting as a source to polarizer) is designed and simulated at around $\simeq$30 GHz. The prototype of both the polarizer and antenna are fabricated and measured. Later, a comparison is made between the simulated and measured results.
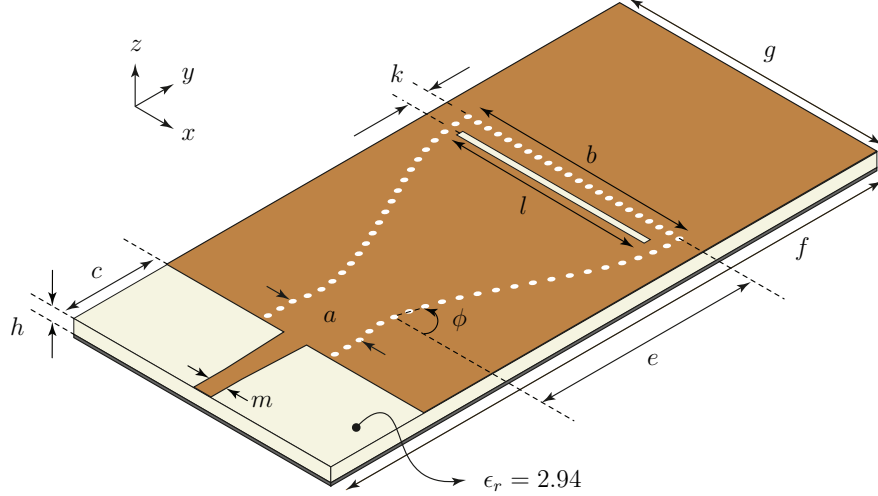
Figure 3.1: 3D view of CS-SIW narrow slot antenna and its corresponding dimensions (in mm) are: $h = 0.508$, $a = 5$, $b = 15.78$, $c = 6$, $e = 13.6$, $f = 28.08$, $g = 19.2$, $k = 1.31$, $l = 14$, $m = 1.28$ and $\phi = 67°$.

3.2 Proposed LP CS-SIW Narrow Slot Antenna

The 3D model of the proposed linearly polarized (LP) CS-SIW narrow slot antenna is shown in figure 3.1. The designed antenna is along the xy plane referenced by the rectangular coordinate system and constructed on a layer of Rogers 6002 substrate with relative permittivity, $\epsilon_r = 2.94 \pm 0.04$, at 10 GHz and loss tangent, $\tan \delta = 0.0012$. The height or thickness of the substrate is, $h = 0.508$ mm, which is along the $+z$ coordinate.

The antenna design is divided into three sections; namely, microstrip line, SIW, and CS-SIW. These sections are involved in the construction of two transitional layers. The transitional layers are essential at the medium discontinuities to minimize the reflections back to the source (see [9], sec 2.6). For an EM wave, traveling from source to radiating element (i.e., slot): the first encountered transitional layer is from, microstrip line to SIW and the second from, SIW to CS-SIW. At first, we shall begin with the construction of the CS-SIW structure and followed by a discussion on the transitional layer(s).

3.2.1 Cylindrical Sector Substrate Integrated Waveguide (CS-SIW)

Consider a SIW structure of width, a, and height, $h \ll \lambda_g/2$, as illustrated in figure 2.5(a). Let the SIW width, a, be fixed at one end, and we shall increase the width (let's say,

b) of the SIW at the other end; such that the width of the SIW is continuously increasing in the transverse plane from $a \rightarrow b$ along the longitudinal direction (which is also the wave propagating direction). The new resulting model is referred to as *cylindrical sector* SIW. The term *sector* corresponds to the area of SIW sidewalls. The term *cylindrical* is prefixed because the waves traveling inside the sectoral SIW has cylindrical equiphase surfaces (see [21], p.29; [22], p.85). Hence, to define the CS-SIW structure, a cylindrical coordinate system is chosen, since CS-SIW sidewalls are along the direction of radius, r, at an angle, ϕ, referenced from the origin $(r = 0, \phi = 0°, z = 0)$.

3.2.2 SIW to CS-SIW

We know from section 2.4, SIW structure support only TE_{m0} above the cut-off frequency. The SIW is designed to operate in Ka-band (26 - 40 GHz) carrying dominant TE_{10} mode only. Thus, when the CS-SIW structure is fed with SIW dominant mode, TE_{10}, the mode inside the CS-SIW is TE_{10}. However, TE_{10} mode in CS-SIW travel radially (along r) and the equiphase surfaces are cylindrical along a ϕz plane. As the CS-SIW sidewall width increases, higher-order modes (such as TE_{20}) can be excited. Therefore, to restrict the excitation of higher-order modes, design parameters that control the CS-SIW sidewall, length, and width are chosen carefully. Further, the CS-SIW is terminated with a short circuit load. As a result, standing waves are formed within the CS-SIW. The normalized electric and magnetic field intensity standing wave patterns for the TE_{10} mode are shown in figures 3.2(a) and 3.2(b), respectively at 30 GHz.

For the standing waves to radiate into free space, a narrow slot was etched on the top metal of the CS-SIW at a distance, k, from the CS-SIW short circuit load. It is indeed complex to calculate the CS-SIW guided wavelength, λ_g, owing to its' non-uniform structure. Therefore, the optimum value for the narrow slots' position, length, and width were studied by simulating the antenna using CST software in parameter sweep mode.

3.2.3 Microstrip Line to SIW

Numerous options are available to excite an SIW structure, for instance, a coaxial probe, microstrip line, Grounded Co-Planar Waveguide (GCPW). However, the transition from the coaxial probe to SIW (see [9], p.214 - although shown by working with rectangular waveguide) is indeed difficult to realize owing to the non-planar structure. Therefore, planar transitions
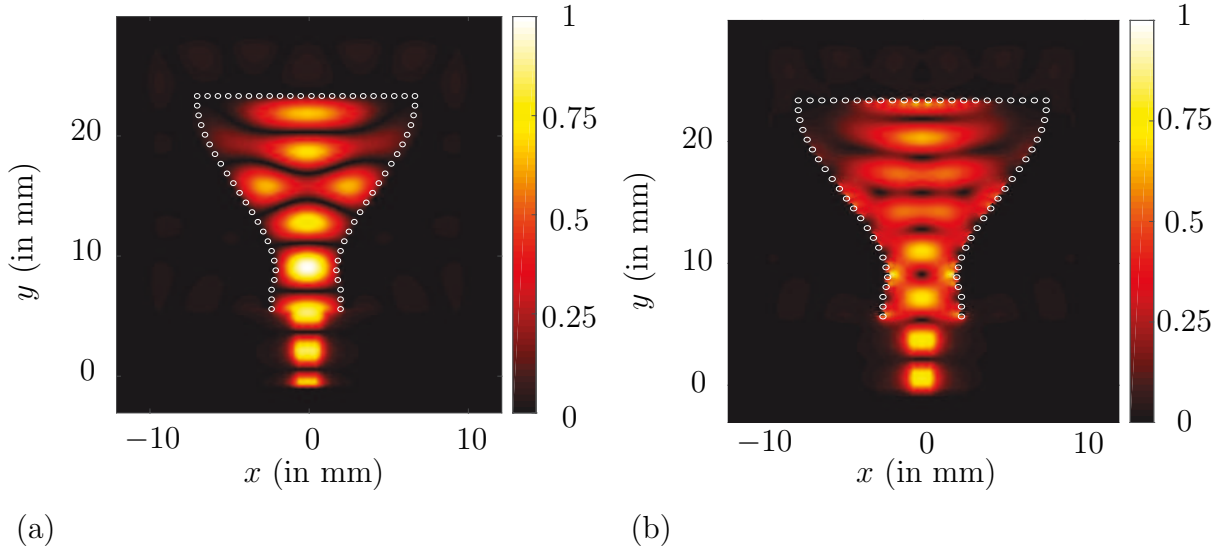
Figure 3.2: (a) Normalized standing wave pattern of the electric field intensity, $|\mathbf{E}|$, (in V/m) inside CS-SIW at 30 GHz; (b) Normalized standing wave pattern of the magnetic field intensity, $|\mathbf{H}|$, (in A/m) inside CS-SIW at 30 GHz.

such as microstrip line or GCPW are preferred as they can be realized on the same substrate along with the antenna.

In this thesis, we have chosen the microstrip line to excite the SIW owing to its' simplicity. Consequently, to understand the reflection and transmission properties, a microstrip - SIW - microstrip transition is designed on Rogers 6002 substrate with $\epsilon_r = 2.94$ at 10 GHz, loss tangent, $\tan\delta = 0.0012$, and thickness, $h = 0.508$ mm using CST software as shown in figure 3.3(a). The width of the microstrip line is calculated to be, m=1.28 mm for $Z_0 = 50\Omega$ (using [9], Eqn. 3.196). The SIW is designed to operate at around 30 GHz. The width, via diameter and the via periodicity of the SIW, are $a = 5$ mm, $d = 0.4$ mm, and $p = 0.8$ mm, respectively. Two wave ports are constructed at the cross-section of the microstrip and are, l, distance apart.

The MS-SIW-MS transition model is simulated using CST software. The transition is symmetry normal to the xz-plane. Thus, simulating $[S]$-parameter for only one-port would suffice. The width of the microstrip line was tapered from, m to b, to match the impedance between SIW and microstrip line. The simulated reflection and transmission coefficient are found to be $<$ -25 dB and $>$ -0.45 dB, respectively as shown in figure 3.3(b). Therefore, the insertion loss is only 0.225 dB ($= 0.45/2$) for a one-sided microstrip to SIW transition across the frequency range 26 - 34 GHz.

(a)   (b)
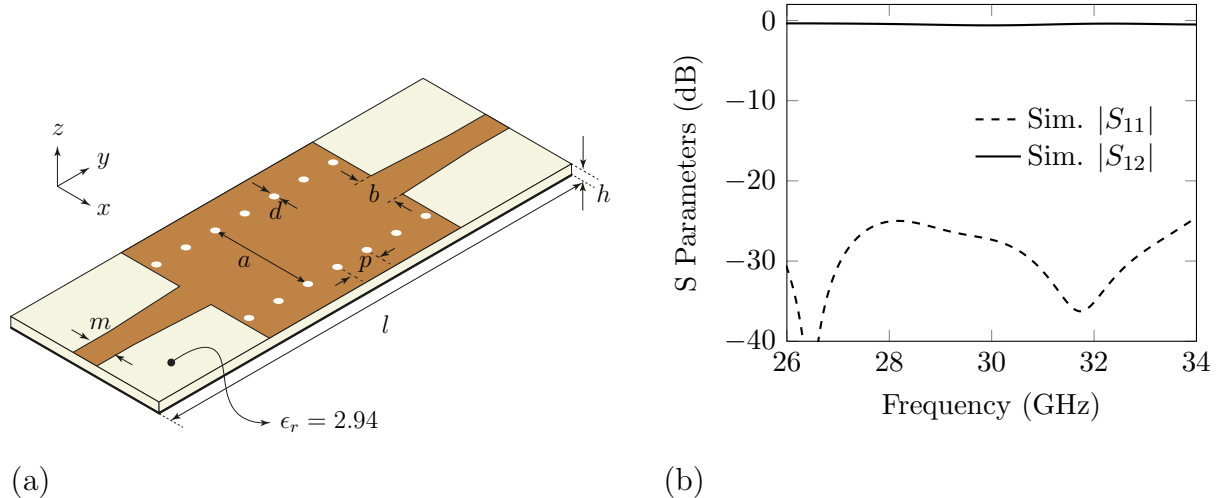
Figure 3.3: MS-SIW-MS transition (a) 3D view and its corresponding dimensions (in mm) are $a = 5$, $b = 1.7$, $d = 0.4$, $h = 0.508$, $p = 0.8$ and $m = 1.28$ (b) Plot of two-port scattering parameters (in dB) versus frequency (in GHz).

3.3 Results and Discussion

The fabricated prototype of the LP CS-SIW narrow slot antenna is shown in figure 3.4, and the end-launch connector is used to measure the antenna. The connector has a characteristic impedance, $Z_0 = 50\ \Omega$. However, for practical applications, the connectors are not required to feed the antenna. The output of the RF component (such as filter, low noise amplifier (LNA) or power amplifier (PA)) is connected with antenna using any methods of the waveguiding structures.

The LP CS-SIW narrow slot antenna model shown in figure 3.1 was also simulated using CST software by designing a waveguide port at the beginning of the microstrip line. The simulated reflection coefficient, $|S_{11}|$, and the realized gain plots versus frequency are shown in figure 3.5(a). As read from figure 3.5(a), the impedance bandwidth of the antenna is from 28.7 - 32.0 GHz, and the calculated fractional bandwidth is found to be 10.87%. The simulated realized gain varies from 8.33 - 8.84 dB, and the simulated radiation efficiency is above 87.22% throughout the impedance bandwidth. The measured antenna properties for the reflection coefficient, $|S_{11}|$ and the realized gain versus frequency are shown in figure 3.5(b).

A frequency shift of 1.02 GHz (= 29.72 - 28.7 GHz) is observed between the measured
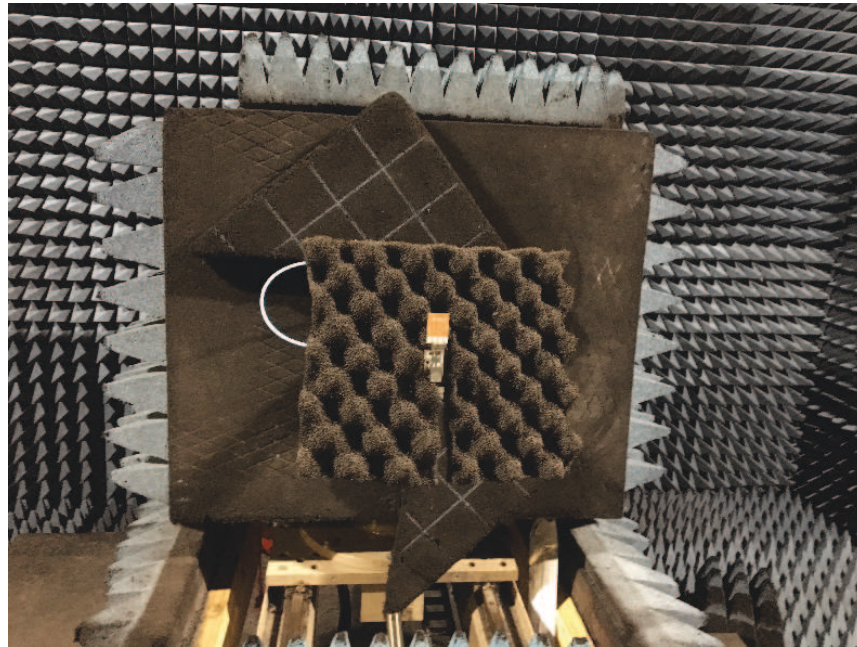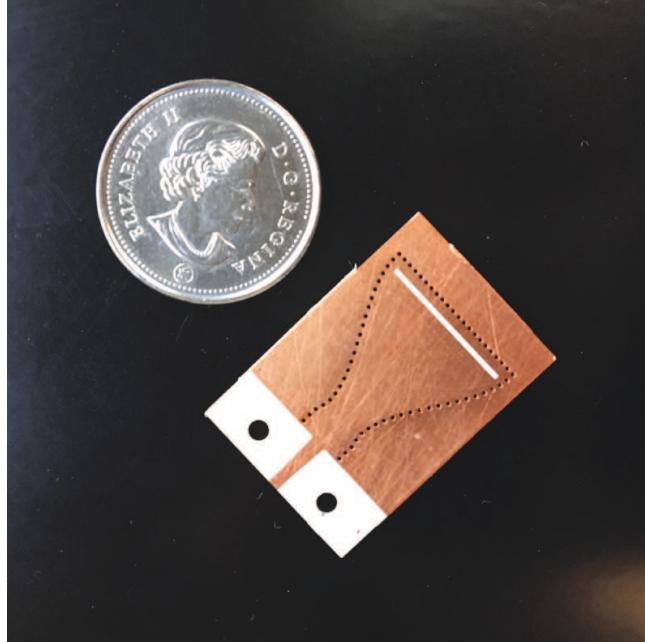
Figure 3.4: (Top) The top-view of CS-SIW narrow slot antenna prototype. (Bottom) The CS-SIW narrow slot antenna, antenna under test (AUT), for radiation pattern measurement inside the anechoic chamber.

(a)   (b)
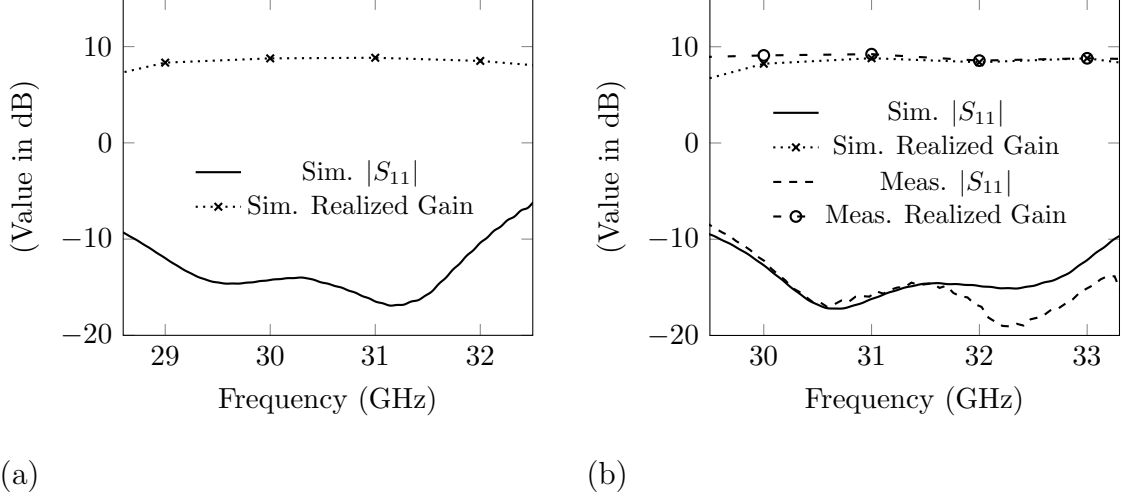
Figure 3.5: LP CS-SIW narrow slot antenna (a) plot of simulated $|S_{11}|$ (in dB) and realized gain (in dB) versus frequency (in GHz) for $\epsilon_r = 2.94$; and, (b) plot of simulated $|S_{11}|$ (in dB) and realized gain (in dB) versus frequency (in GHz) for $\epsilon_r = 2.7$.

and the simulated reflection co-efficient, $|S_{11}|$. The shift in the frequency could be due to the change in relative permittivity, ϵ_r, of the Rogers 6002 substrate used during fabrication. To validate this behavior, the ϵ_r of the Rogers 6002 substrate was varied and simulated using CST software. Thus, when $\epsilon_r = 2.7$ (8.5% change), the simulated[1] and the measured, $|S_{11}|$ for the CS-SIW narrow slot antenna are close to each other as shown in figure 3.5(b). The measured realized gain varies from 8.56 - 9.1 dB over the impedance bandwidth.

The complex input impedance (in Ω) of the LP CS-SIW narrow slot antenna versus frequency (in GHz) is shown in figure 3.6(a),(b). The plot of normalized electric field intensity, E_y (in V/m), inside the slot versus slot length, l, (in mm) at 30 GHz, 31 GHz, 32 GHz, and 33 GHz are shown in figure 3.6(c) and finally, the plot of impedance bandwidth (in %) versus slot length, l, (in mm) is shown in figure 3.6(d).

The simulated and measured normalized E-plane and H-plane radiation patterns[1] for the CS-SIW narrow slot antenna at multiple frequencies are shown in figure 3.7.

The ripple effect for the simulated E-plane radiation pattern is less when compared to measured because the simulated antenna using CST was analyzed and excited with waveguide

---

[1]For all the antenna designs discussed in the future chapters; the plot of simulated reflection coefficient, realized gain and principal radiation patterns are depicted for Rogers 6002 substrate with relative permittivity, $\epsilon_r = 2.7$.

[1]A compact range anechoic chamber is used for all the antenna pattern measurements at Polytechnique Montreal University
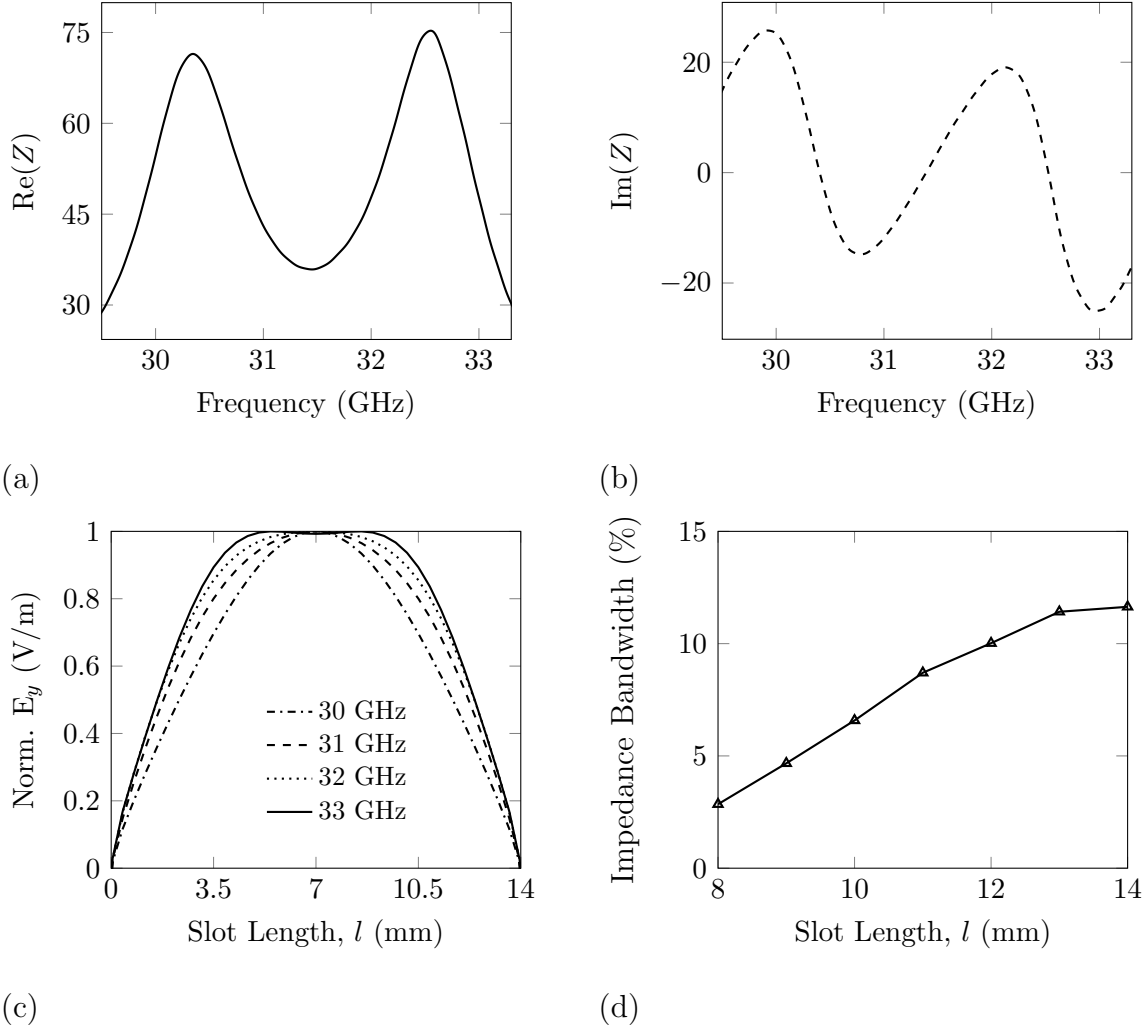
Figure 3.6: (a) and (b) Plot of complex input impedance (in Ω) versus frequency (in GHz), (c) plot of normalized electric field intensity, E_y, (in V/m) inside the slot versus slot length, l, (in mm) at various frequencies, and (d) plot of impedance bandwidth (in %) versus slot length, l, (in mm).

port (but not with connector). The ripples observed in the measured E-plane radiation pattern are due to the presence of end launch connector (constructed using metal) and localized edge diffraction (see [1], p.730). The size of the connector[2] is equal to $10.34 \times 8.89 \times 8.15$ mm^3, which is comparable to the λ_0 at 30 GHz.

The EM waves emanating from the slot, travel along the y-axis (as planar conductor act as a hard surface [23]). The waves then impinge on a connector producing induced currents and the fields are scattered in arbitrary directions, which may sum up either constructively

---

[2]https://mpd.southwestmicrowave.com/wp-content/uploads/2018/06/1092-01A-9.pdf

Freq. (GHz)	Norm. E-plane (dB)	Norm. H-plane (dB)
30		
31		
32		
33		
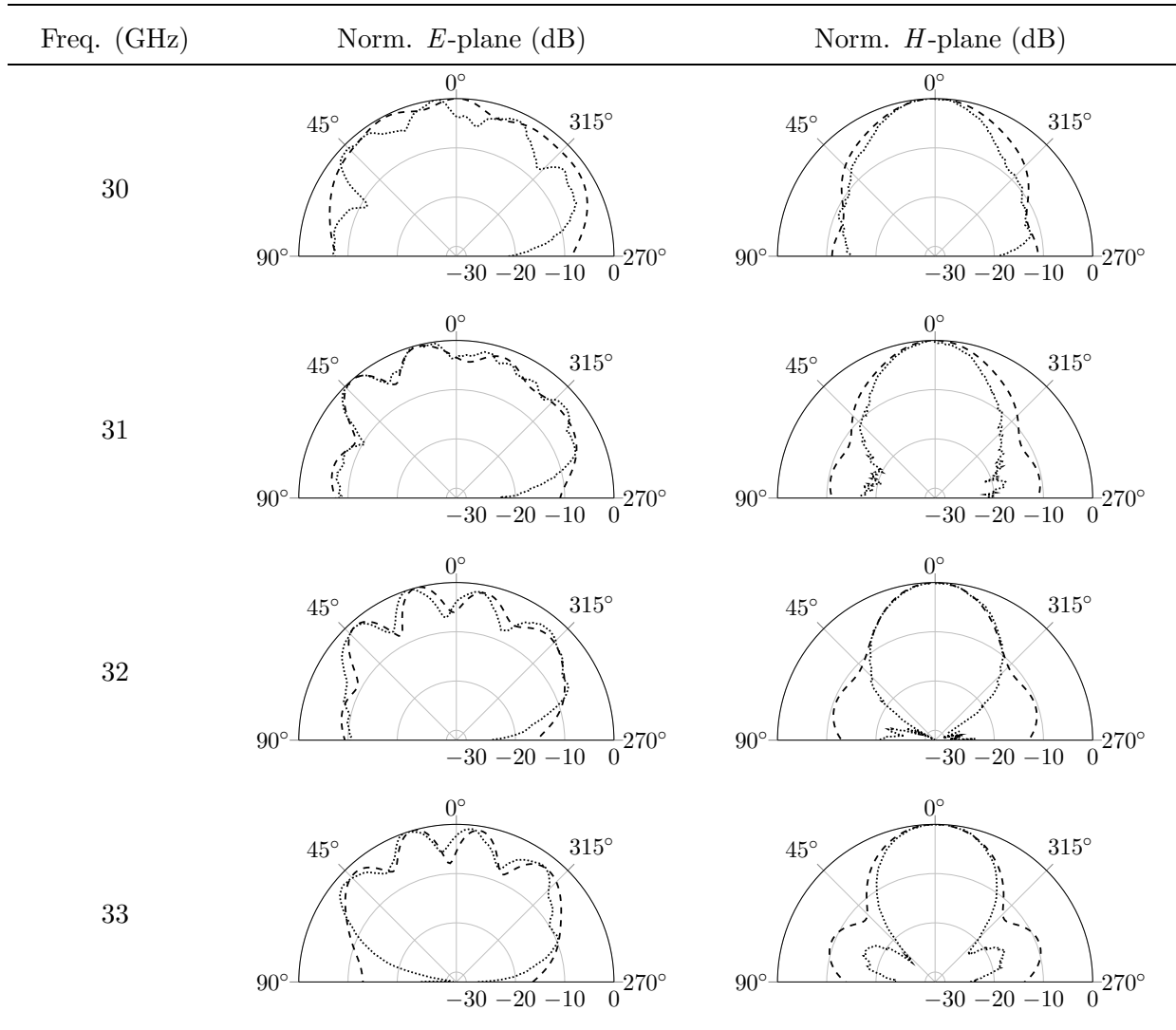
Figure 3.7: Measured (dotted) and simulated (dashed) normalized radiation patterns (E-plane ($\phi = 90°$) and H-plane ($\phi = 0°$)) for CS-SIW narrow slot antenna at multiple frequencies.

or destructively with the E-field radiating from the slot. Two methods can be employed to reduce the ripple effect namely: (1) increase the distance between the connector and radiated fields from the slot, and (2) to construct a soft surface on the top layer of the antenna.

However, the ripple effect is not observed for the radiated H-field because the connector and H-field are orthogonal to each other. Thus, simulated and measured normalized H-plane radiation pattern is not disturbed at all the frequencies, as illustrated in figure 3.7.

3.4 Proposed LP CS-SIW Narrow Slot Antenna for Gain Improvement

A top layer consisting of rectangular copper slabs and an electromagnetic bandgap (EBG) unit cells are constructed using Rogers 3003 ungrounded substrate, to further increase the gain of the LP CS-SIW narrow slot antenna as shown in figure 3.8.

The relative permittivity, ϵ_r, loss tangent, $\tan\delta$ and the thickness, c_2 of the Rogers 3003 substrate are 3 ± 0.04 at 10 GHz, 0.001 and 0.787 mm, respectively. The top substrate is symmetrical along xz plane, and its' dimensions are $e_2 \times f_2$. The substrate is placed on top of the CS-SIW slot antenna at a point, $P = (e_2/2, f_2/2)$. The point, P is also equal to the slot center position. For the EM fields to radiate from the slot, the volume $(a_2 \times b_2 \times c_2 \text{ mm}^3)$ of the Rogers 3003 substrate is hollow. Distance, b_2, separates the two rectangular slabs. For each slab, two rows of via are constructed. The length, diameter and the periodicity of the via are c_2, 0.4 mm and 0.8 mm, respectively. The via connects the top layer of the slot with the rectangular slab; this whole region acts as a volume made of copper. The dimensions of each copper volume are $(d_2 - b_2)/2 \times a_2 \times c_2 \text{ mm}^3$.

The analysis for the antenna model shown in figure 3.8 is as follows. The EM fields radiated from the slot travels along the broadside (i.e., $+z$) direction. These radiated fields produce an induced current when incident on the rectangular slab. Since the radiated **H** fields from the slot are along x axis, the induced currents on the slab are along y direction (by applying PEC boundary condition). The width of the slab is designed to be a quarter wavelength at the center frequency of antenna operation. The quarter wavelength acts as an open and short circuit load, and the standing waves are formed along y axis. Using image theory for the slab **E** field distribution, we can replace the slab with a magnetic current. These magnetic currents act as a secondary radiating source and help in increasing the gain of the antenna by adding constructively with the slot's radiation (which acts as primary radiating source). This technique to increase the gain of the antenna is shown in [24, 25].

3.4.1 Design of EBG Unit Cell

The motivation of designing electromagnetic bandgap (EBG) unit cells on the top layer, is to reduce the ripple effect for the principal E-plane radiation pattern, as observed in figure 3.7. The radiated fields from the slot can be limited by designing an artificial magnetic
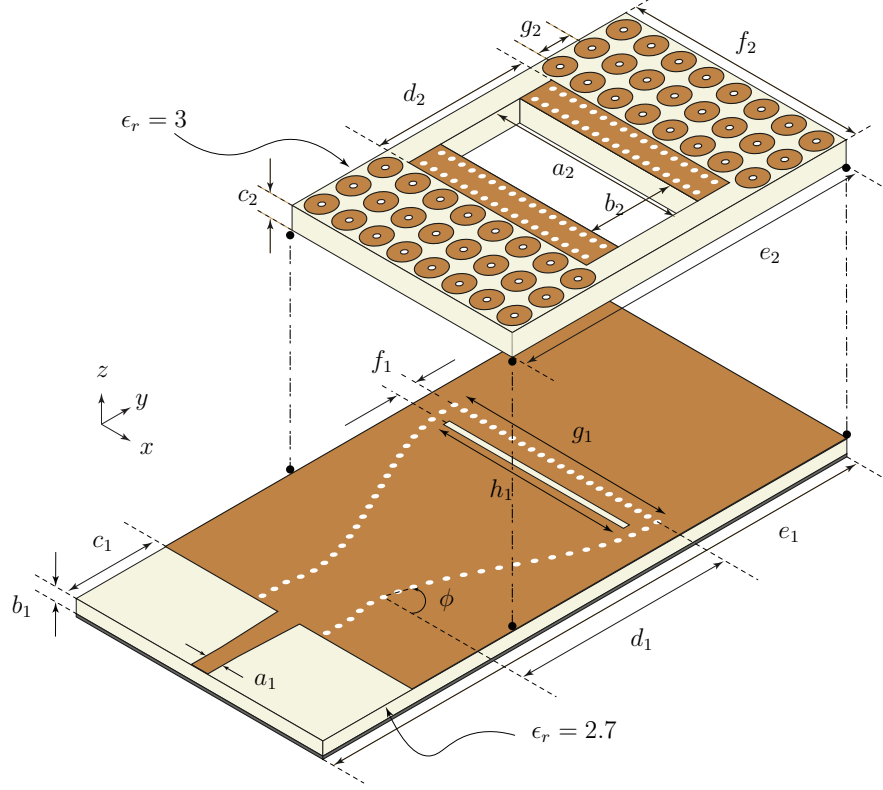
Figure 3.8: Multilayer CS-SIW narrow slot antenna for improving gain and its corresponding dimensions (in mm) are: $a_1 = 1.28$, $b_1 = 0.508$, $c_1 = 6$, $d_1 = 14.4$, $f_1 = 1.31$, $h_1 = 14$, $g_1 = 15.87$, $e_1 = 35.29$, $c_2 = 0.787$, $d_2 = 10.8$, $a_2 = 15.5$, $b_2 = 6$, $e_2 = 24$, $f_2 = 19.2$, $g_2 = 2.4$, and $\phi = 67°$.

conductor (AMC) [26]. An AMC is an engineered structure offering high impedance surface by designing a group of periodic EBG unit cells. These structures are created because the perfect magnetic conductor (PMC) doesn't exist in nature. However, AMC's provide a high impedance surface only to a range of frequencies, due to their periodicity.

Therefore, designing an AMC surface within the frequency band of interest is crucial. To achieve the bandgap phenomenon (or a high impedance surface) for the overall LP CS-SIW narrow slot antenna impedance bandwidth, an EBG unit cell is modeled and simulated using CST software by eigensolver method as shown in figure 3.9(a). The *periodic* boundary conditions are along the x and y axis, and the PEC ($\mathbf{E}_{tan} = 0$) boundary conditions are at z_{min} and z_{max} of the unit cell. The height of the z_{max} is λ_0 from the circular patch (where λ_0 is the free space wavelength at the CS-SIW slot antenna center frequency). The simulated EBG unit cell dispersion diagram is depicted in figure 3.9(b). As read from figure 3.9(b), the designed EBG unit cell act as high impedance surface between 20 - 35 GHz frequencies. The
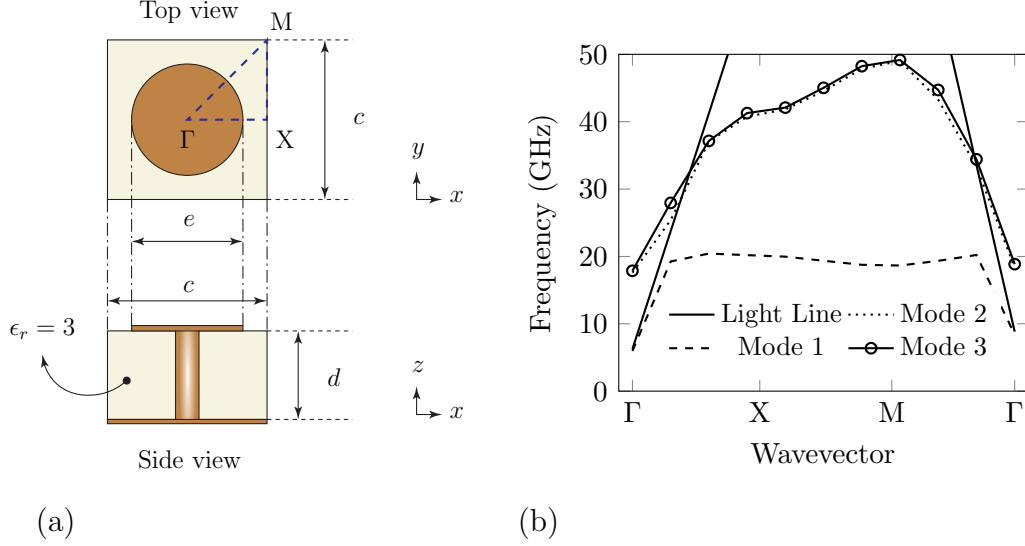
Figure 3.9: (a) Top and Side view of the designed EBG unit cell and its corresponding dimensions (in mm) are $c = 2.4$, $d = 0.787$ and $e = 2$ (b) Dispersion diagram for the designed and simulated EBG unit cell. The band-gap phenomenon is observed from 20 - 35 GHz.

wave vector's, Γ, X, and M in figure 3.9(b) represent imaginary right angle triangular region on the EBG unit cell. This region is known as irreducible Brillouin zone. Since the EBG unit cell is periodically extending in both x and y axis, the phase variation of the guided waves on the unit cell surface along the x axis is plotted from Γ to X. Similarly, the phase is plotted from X to M for the y axis , and M to Γ for both x and y axis (i.e., the diagonal line).

3.4.2 Results and Discussion

The fabricated prototype of the two-layer CS-SIW narrow slot antenna is shown in figure 3.10, and the measurements were taken for $|S_{11}|$, gain and radiation patterns by sweeping frequency range for about ± 3 GHz at 31 GHz. The top and bottom substrates are glued with a layer of epoxy ($\epsilon_r \neq 1$).

The antenna model shown in figure 3.8 was designed and simulated with end-launch connector using CST software. The plot of simulated and measured $|S_{11}|$ (in dB) versus frequency (in GHz) is shown in figure 3.11(a). The simulated impedance bandwidth of the antenna is from 30 - 33.3 GHz, and the calculated fractional bandwidth is 10.42%. A frequency shift of 0.3 GHz is observed between the measured and simulated $|S_{11}|$; this shift
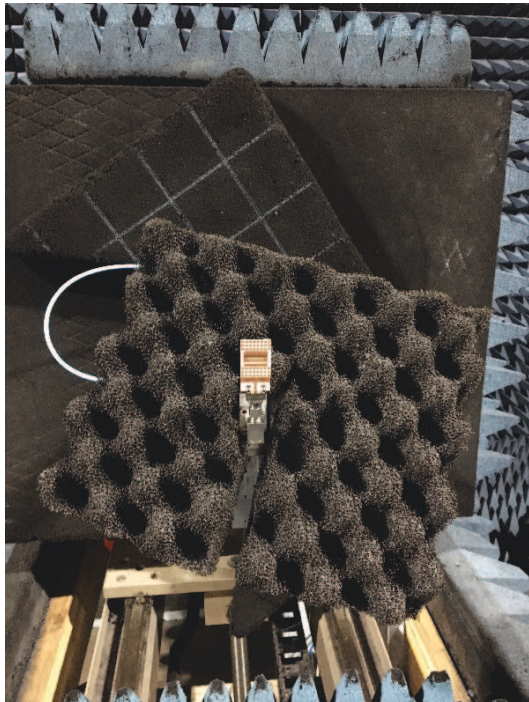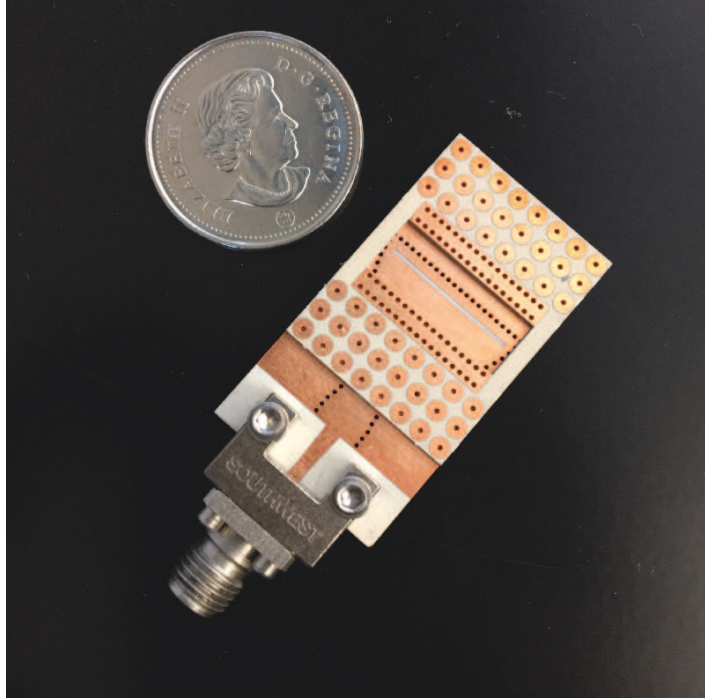
Figure 3.10: (Top) The top-view of the multi-layer CS-SIW narrow slot antenna prototype. (Bottom) The multi-layer CS-SIW narrow slot antenna for radiation pattern measurement inside the anechoic chamber.
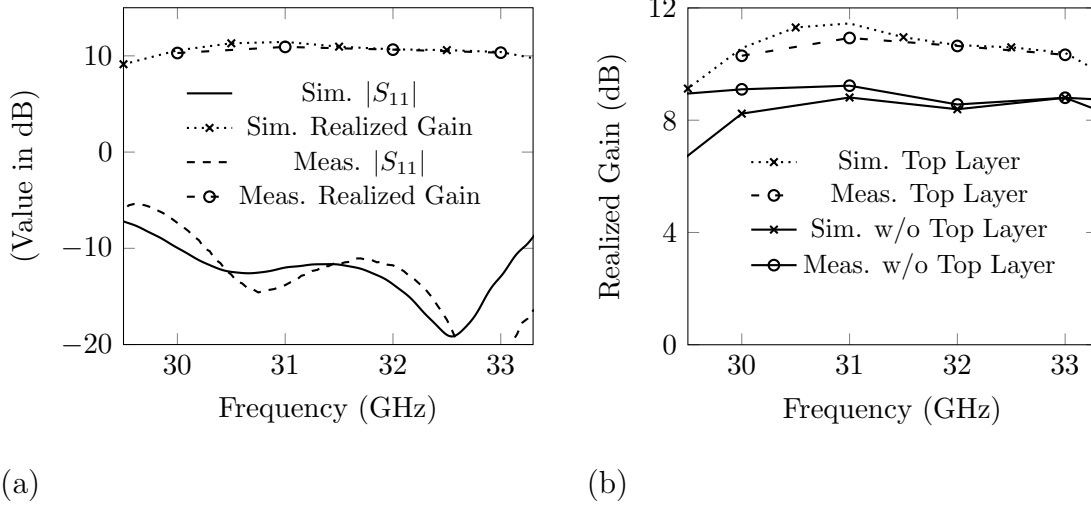
Figure 3.11: (a) Plot of simulated and measured reflection coefficient, $|S_{11}|$, (in dB) and realized gain (in dB) versus frequency (in GHz) for the CS-SIW narrow slot antenna gain improvement; and (b) Comparison between simulated and measured realized gain (in dB) versus frequency (in GHz) for with and without top layer.

could be due to the epoxy substance (wasn't considered during simulation). Both simulated and measured reflection coefficients are around -10 dB, which we find acceptable.

The simulated gain of the antenna is in between 10.5 - 11.44 dB for the overall impedance bandwidth, while, the measured realized gain of the antenna is the range 10.29 - 10.9 dB. The maximum gain for the measured antenna is observed at 32 GHz. The realized gain comparison plots for with and without top layer is as shown in figure 3.11(b). Thus, the presence of the top layer increases the gain of the single-layer CS-SIW narrow slot antenna by 2.1 to 2.7 dB over the impedance bandwidth.

The principal E and H plane normalized radiation patterns for the multi-layer CS-SIW slot antenna are depicted in figure 3.12 at 30, 31, 32, and 33 GHz. The ripple effect is observed for both the simulated and measured principal E plane patterns due to the presence of the connector at a shorter distance to the slot. However, by increasing the distance between the connector and the slot the ripple effect can be further reduced. Consequently, we can also extend the AMC surface to a comparable wavelength along y-axis. The simulated and measured, normalized H plane patterns are similar to each other across frequencies.

Freq. (GHz)	Norm. E-plane (dB)	Norm. H-plane (dB)
30		
31		
32		
33		
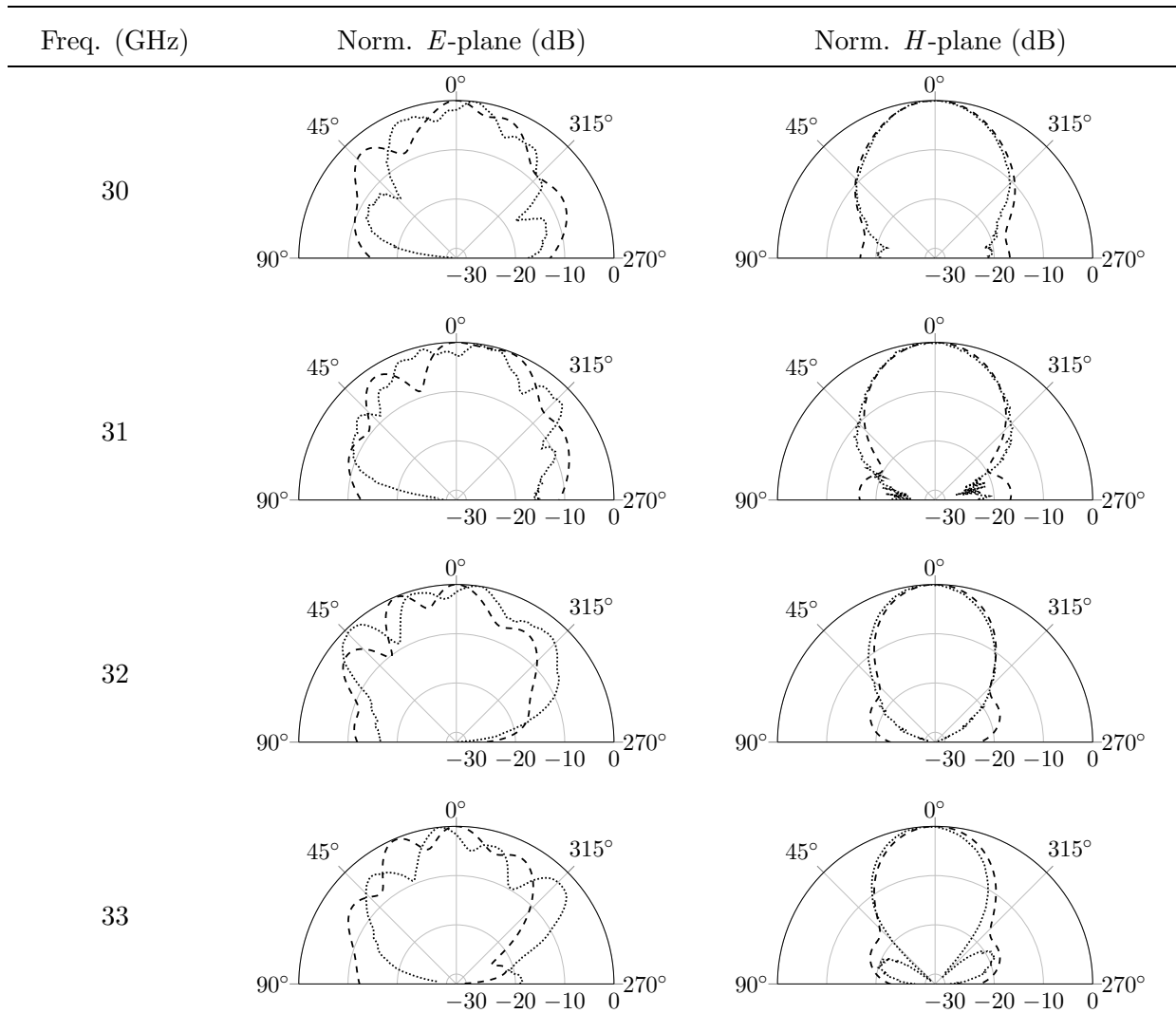
Figure 3.12: Measured (dotted) and simulated (dashed) normalized radiation patterns (E-plane ($\phi = 90°$) and H-plane ($\phi = 0°$)) for CS-SIW slot antenna gain improvement at multiple frequencies.

3.5 Comparsion With Other mm-wave Antennas

The table 3.1 depicts the comparison between CS-SIW narrow slot antenna (with and without top-layer) with other mm-wave antennas available in the literature. As read from the table 3.1, the proposed CS-SIW slot antenna's characteristic in terms of both impedance bandwidth and the peak gain are higher when compared with other SIW slot antenna models.

Ref.	Freq. (GHz)	Impedance Bandwidth (%)	Peak Gain (dB)	X-pol (dB)	Dimension (in λ_0)
[27]	28	10.2	6.48	30	$0.8 \times 0.6 \times 0.09$
[28]	38	15.6	6.5	20	$0.7 \times 0.9 \times 0.06$
[12]	10	1.7	5.4	16.1	$0.7 \times 0.8 \times 0.02$
[13]	10	9.4	5.4	15	$0.9 \times 0.6 \times 0.03$
[15]	60	11.6	7.9	-	$2 \times 0.4 \times 0.13$
[29]	60	26.4	5.57	-	$2.8 \times 3.2 \times 0.22$
[30]	28	8.7	7.5	-	$2.8 \times 1.9 \times 0.07$
[31]	28	8.8	12.4	-	$1.9 \times 1.05 \times 0.6$
CS-SIW Slot (single layer)	30	**10.87**	**8.84**	16	$2.8 \times 1.6 \times 0.05$
CS-SIW Slot (multi layer)	30	**10.42**	**11.44**	18.2	$3.5 \times 1.9 \times 0.13$

Table 3.1: Proposed CS-SIW slot antenna's characteristic comparison with other works.

3.6 Proposed CP CS-SIW Narrow Slot Antenna using Meander-line Polarizer

3.6.1 Introduction

Circularly polarized antennas are advantageous over linearly polarized antennas due to a reduced effect on, multipath interference, and polarization mismatch losses.

The transmitted RF signal can take multiple paths to reach the receiver. At mm-wave frequency, the number of multiple paths increases in the dense urban environment due to readily available high reflective materials such as glass, concrete, etc [4]. For simplicity to understand the multipath phenomenon, let us consider only two signal paths by ignoring all the other possible paths between the transmitter and receiver. Let the two paths be line-of-sight (LOS) and non-line-of-sight (NLOS). An NLOS is a path between the transmitter (Tx) and the receiver (Rx) where the signal undergoes reflection due to obstacles, such as buildings. When both Tx and Rx are linear polarized (LP) antennas, the signal propagating in the LOS path and NLOS path can be out-of-phase with each other when they reach the Rx at the same time. The out-of-phase causes signal degradation and decreased throughput. As a result, minimizes multipath effect by using circularly polarized (CP) antennas at Tx and Rx. Because, the LOS path and NLOS path are two different waves; and the Rx CP antenna simply ignore (or reject) the wave coming from NLOS path due to complete polarization mismatch (see [32], p.1).

The second advantage of CP antennas are - the orientation of the CP antenna at both Tx and Rx won't result in polarization mismatch loss, p, (i.e., $p = 1$) as long as both the CP antenna at the Tx and Rx have the same polarization. However, the orientation of the LP antennas at the Tx and Rx is critical, and polarization mismatch loss can value from $0 \leq p \leq 1$. $p = 0$. Thus, $p = 0$ implies a complete mismatch between the orientation of the Tx antenna and Rx antenna (see [1], sec 4.4.5),(see [32], p.1).

In general, a CP antenna is categorized into two types, namely RHCP and LHCP, depending on the sense of rotation of the polarization. RHCP stands for right-hand circularly polarized, and LHCP stands for left-hand circularly polarized. The curl of the electric field and Poynting vector is used to identify RHCP or an LHCP antenna. Few work on the meander-line polarizer has been already covered in the literature [33–35]. This section serves only as a proof of concept for transforming linearly polarized waves to circularly polarized
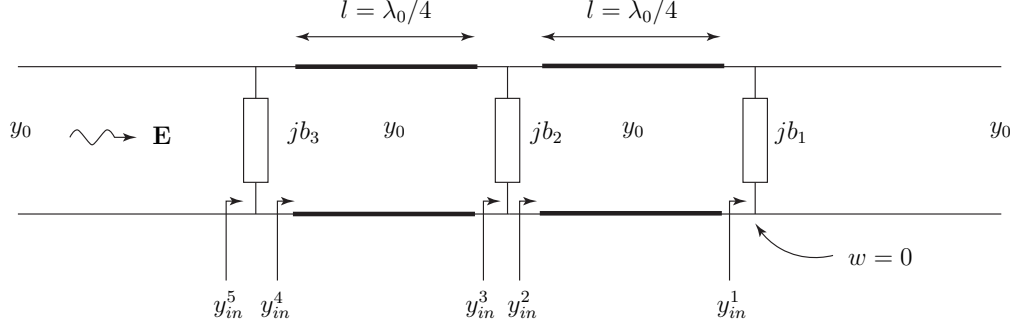
Figure 3.13: Normalized equivalent transmission line model for the three layer stacked meander-line polarizer, where $y_0 = Y_0/Y_0 = 1$, $jb_m = jB_m/Y_0$, and $y_{in}^n = Y_{in}^n/Y_0$.

waves at mm-wave frequencies.

3.6.2   Theory of Meander-line Polarizer

The theory of meander-line polarizer is given in (see [36], Appendix C). We shall revisit and review three-layer meander-line polarizer only in this thesis.

Figure 3.13 depicts the normalized equivalent transmission line model for a three layered stacked meander-line polarizer. jb_1, jb_2 and jb_3 denote the normalized shunt susceptance for each layer. Both negative and positive values are possible for shunt susceptance, b, as mentioned in single layer meander-line polarizer. Depending on the orientation of the electric field concerning the meander-line trace, we have the privilege to replace the shunt component with respective distributive passive components (either inductor or capacitor). If the **E** component is parallel to the meander-line trace, the shunt component is an inductor, and if **E** component is perpendicular to the meander-line trace, the shunt component is a capacitor. Many alternate methods (such as transmission line theory, $ABCD$ matrix (using cascaded network approach), Smith chart) can be used in solving the two-port reciprocal network illustrated in figure 3.13.

We shall assume that the electric field component is parallel to the meander-line trace. Thus, the susceptances, jb_1, jb_2, and jb_3 are inductive for figure 3.13. We shall employ a Smith chart to analyze the equivalent transmission network at the center frequency, f_0. The value of the susceptance, jb_1, jb_2, and jb_3 are chosen such that the total phase shift for the equivalent circuit yields $45°$. The input admittance, y_{in}^1, and y_{in}^2 can be marked on the admittance Smith chart as illustrated (on the left-hand side) in figure 3.14. By using the
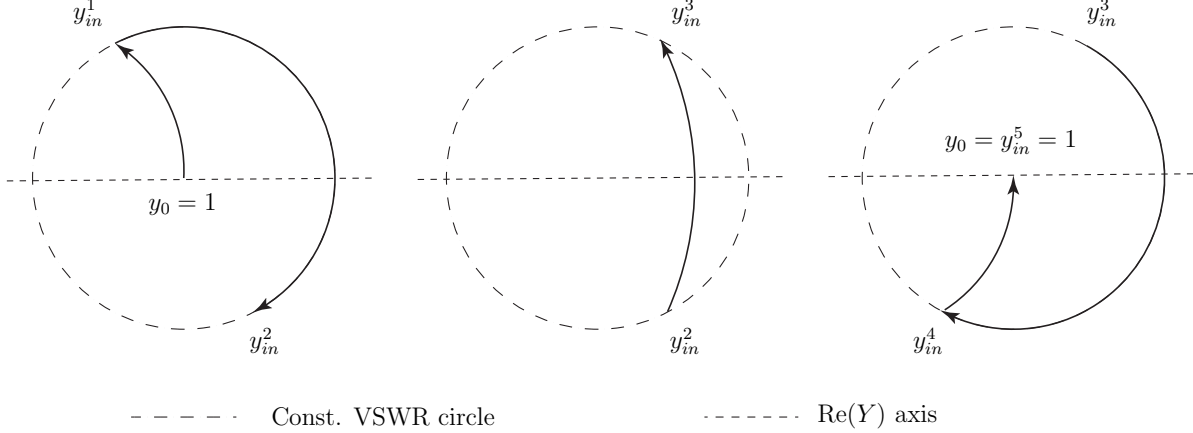
Figure 3.14: Three layered meander-line equivalent circuit analysis at center frequency, f_0, using admittance Smith chart for inductive susceptances, jb_1, jb_2 and jb_3.

quarter-wave transmission line, the input admittance, y_{in}^1, is transformed to, y_{in}^2, by moving along the constant VSWR (Voltage Standing Wave Ratio) circle. The susceptance, jb_2, is chosen such that its value is $(jb_1)/2$. Therefore, the point from y_{in}^2 to y_{in}^3 has moved along the constant conductance circle anti-clockwise. By using another quarter-wave transmission line, the input admittance value has moved from y_{in}^3 to y_{in}^4. Finally, the value of the jb_3 is equal to jb_1, and thus we reach to a matched load as shown (on the right-hand side) in figure 3.14. Since, the phase$(jb_1 + jb_2 + jb_3) = 45°$ and $jb_2 = (jb_1)/2 = (jb_3)/2$, the phase shift provided by the jb_2 is double that of jb_1 or jb_3. Therefore, jb_2 produces a 22.5° phase shift and, jb_1 and jb_3 produce an 11.25° phase shift at the center frequency, f_0. A similar analysis can be used for the electric field component perpendicular to the meander-line trace and replacing the shunt component with a capacitor (having susceptances, $b_n > 0$).

3.6.3   Design of Meander-line Polarizer Unit Cell

A three-layer meander-line unit cell is designed using CST software, as shown in figure 3.15(a). The stacked unit cell layers are parallel to the w-axis, and the distance between two consecutive layers is 2.246 mm ($\simeq \lambda_0/4$ where $\lambda_0/4$ is the free space wavelength at 30 GHz). Each unit cell layer comprises of a meander-line trace and a dielectric substrate. The thickness of the meander-lines is too thin (about 17.5 μm) and is indeed challenging to stack multiple standalone meander-line trace on top of each other in free space. Hence, each meander-line is backed or supported by Rogers 3003 dielectric substrate. The substrate has a relative permittivity, $\epsilon_r = 3 \pm 0.04$ at 10 GHz, loss tangent, $\tan \delta$=0.001, and substrate
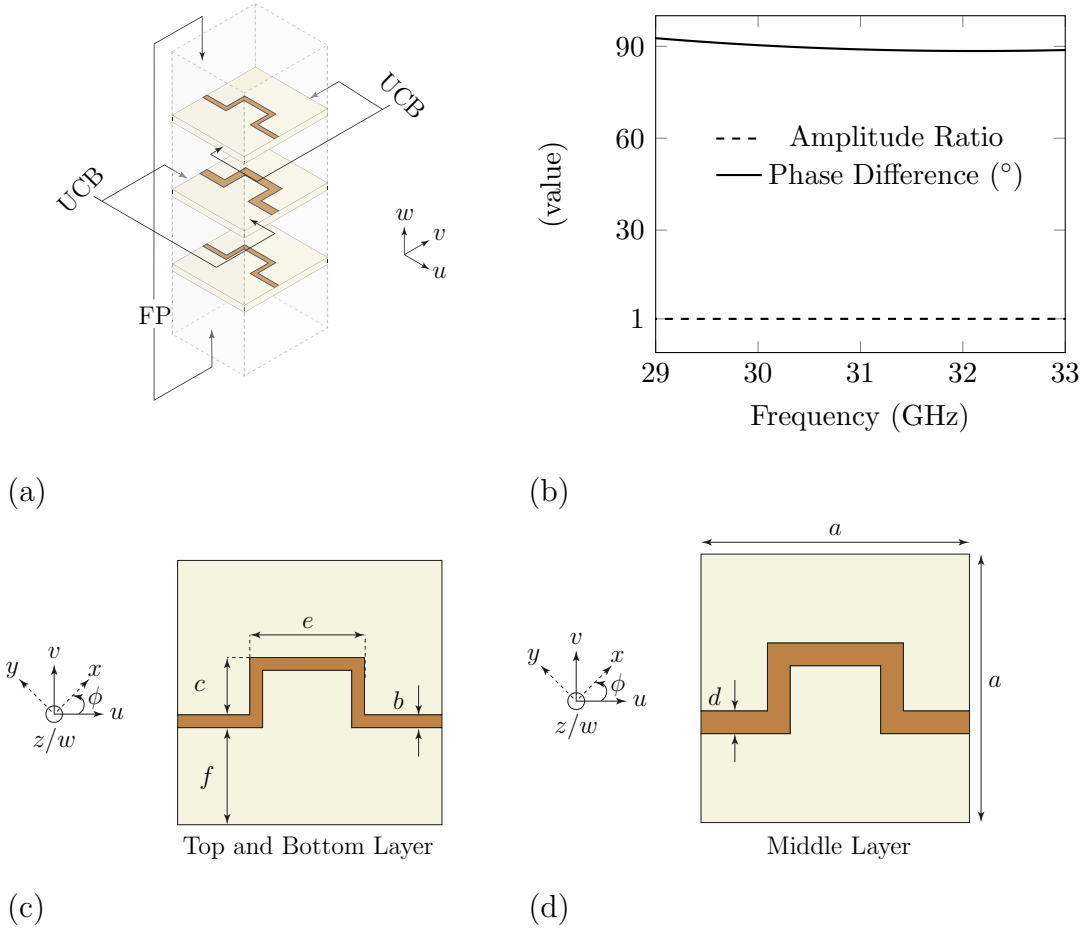
Figure 3.15: (a) 3D view of three layered meander-line polarizer unit cell. 'UCB' represent 'Unit Cell Boundary' and 'FP' represent 'Floquet Port', (b) Amplitude ratio and phase difference (in degree) of TE, TM mode versus frequency (in GHz), (c) Top and bottom layer of the designed unit cell, and (d) Middle layer of the designed polarizer unit cell. Meader-line polarizer's unit cell dimension's (in mm) are: $a = 4.15$, $b = 0.2$, $c = 0.9$, $d = 0.35$, $e = 1.8$, $f = 2.075$, and $\phi = 45°$.

thickness is equal to 0.254 mm. The dimensions of the unit cell width and the length are $0.415\lambda_0 \times 0.415\lambda_0$ (where λ_0 is the free space wavelength at 30 GHz). The top view of the individual meander-line unit cell layers is shown in figure 3.15(c) and 3.15(d); and are aligned on the uv axis. The planes normal to both the $\pm u$ axis and $\pm v$ axis are assigned with 'Unit Cell' boundaries (which is similar to the periodic boundary), and the 'Open' boundary is assigned normal to $\pm w$ axis for a three-layered meander-line unit cell as shown in figure 3.15(a).

At first, we shall assume two plane waves that are traveling in the $+w$ direction. Let the
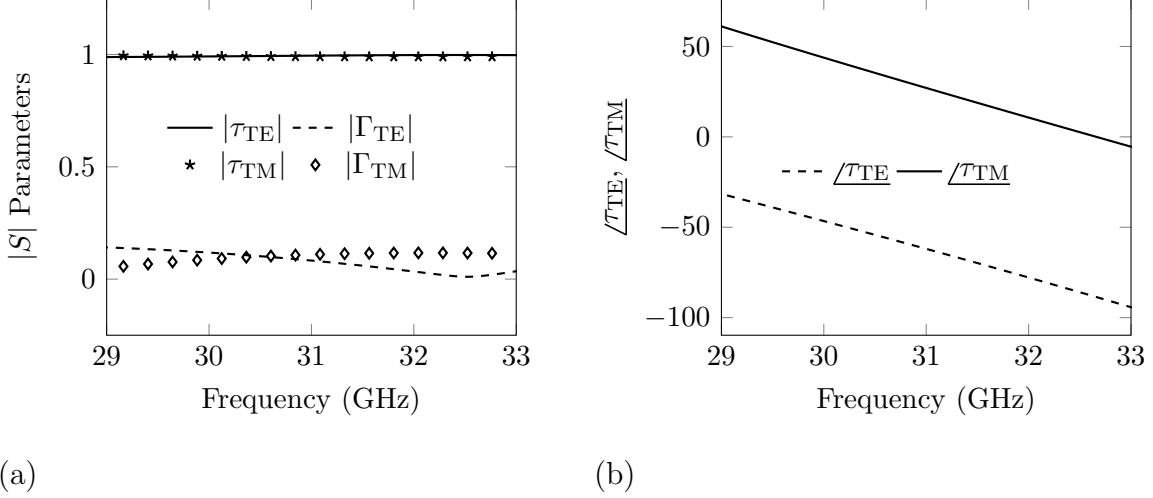
Figure 3.16: Three layered meander-line polarizer unit cell (a) plot of |TE|, |TM| reflection and transmission coefficients versus frequency (in GHz); (b) plot of TE and TM transmission coefficients phase (in deg) versus frequency (in GHz).

E of the two uniform plane waves be orthogonal to each other, and the two waves impinge on the bottom layer of the meander-line polarizer. Hence, the two wave ports normal to the w axis are defined to generate TE and TM modes using 'Floquet boundaries' in CST software. For the TE mode, the electric field component is parallel to the v axis. While, the electric field component is perpendicular to the v axis, for the TM mode. The designed polarizer unit cell, as shown in figure 3.15(a) is simulated using CST under a frequency-domain solver.

For a single port analysis of a two-port network, a total of 8 combinations of scattering parameters are possible. Four out of eight combinations are trivial, due to the TE-TM mode mismatch at the source and destination ports. The remaining four scattering parameters belong to the reflection coefficient, Γ, and the transmission coefficient, τ, when both the source and destination ports are possessing either a TE mode or TM mode. The simulated results for TE, TM mode reflection and transmission parameters in terms of magnitude and phase are depicted in figure 3.16(a) and (b). The plot of the reflection coefficient phase for the TE and TM mode is omitted due to its least importance. The amplitude ratio and the difference in phase between the TE mode and TM mode can now be calculated using equation (3.1) from the obtained transmission scattering parameters (i.e., τ_{TE} and τ_{TM}).

$$\tau_{\text{amplitude\_ratio}} = \frac{|\tau_{\text{TE}}|}{|\tau_{\text{TM}}|} \qquad \tau_{\text{phase\_difference}} = \left|\angle\tau_{\text{TE}}\right| + \left|\angle\tau_{\text{TM}}\right| \qquad (3.1)$$

39
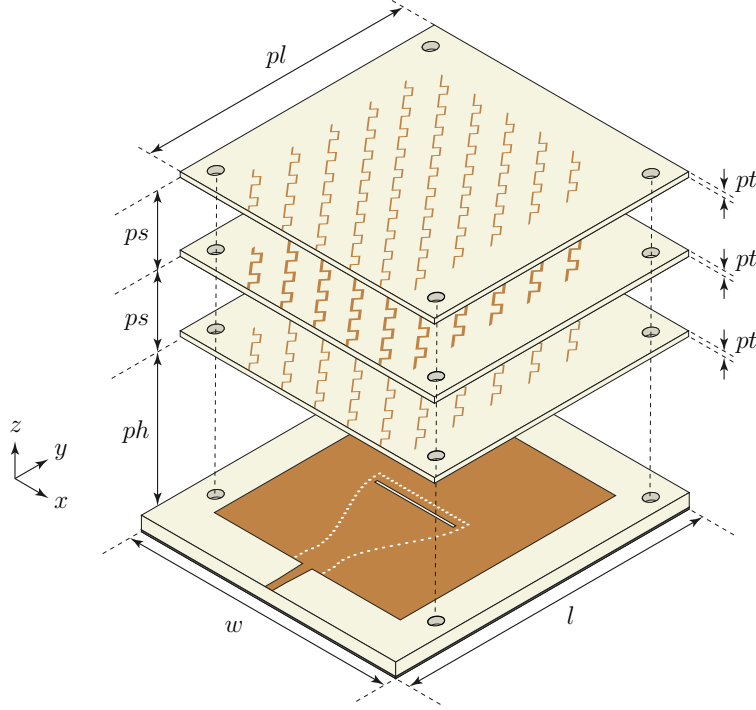
Figure 3.17: 3D view of circularly polarized CS-SIW slot antenna using meander-line polarizer. And, the corresponding antenna dimension's (in mm) are as follows: $ps = 2.5$, $pt = 0.254$, $ph = 4.02$, $pl = 39.11$, $w = 45.2$ and $l = 45.2$.

Using equation (3.1) and the values obtained from figure 3.16(a) and (b), the plot of $\tau_{\text{amplitude\_ratio}}$ and $\tau_{\text{phase\_difference}}$ versus frequency (in GHz) is shown in figure 3.15(b). As read from figure 3.15(b), the amplitude ratio and the difference in phase for both TE mode and TM mode are equal to 1 and are close to $90°$ (with the variation of $\pm 2.5°$ across the frequency range 29 - 33 GHz), respectively. Consequently, to achieve the desired amplitude ratio and the difference in phase, incremental changes were applied to the unit cell parameters and analyzed using CST software.

3.6.4 Design and Analysis of CS-SIW Slot Antenna using Meander-line Polarizer

The CS-SIW narrow slot antenna using a three-layered meander-line polarizer is aligned on the xy plane of the rectangular coordinate system as shown in figure 3.17. Each layer of the designed meander-line polarizer unit cell shown in figure 3.17(a) is extended periodically to a finite $(w/2 \times l/2)$ size along $\pm$u and $\pm$v axis. The finite-sized, *polarizer*, is rotated by $+45°$ and is placed on top of CS-SIW slot antenna at a distance equal to, ph. Indeed, it is

40

mandatory to rotate the polarizer by $\pm 45°$, so that the radiated E-field from the CS-SIW narrow slot antenna can be divided into two equal and orthogonal components (from the theory of vector identities). These two orthogonal components are parallel and perpendicular to the aligned meander lines. As in this case, when the polarizer is rotated by $+45°$ we transform LP to the LHCP wave, and if the polarizer is rotated by $-45°$, we transform LP to the RHCP wave.

3.6.5 Results and Discussion

The prototype of the linearly polarized CS-SIW narrow slot antenna and the three-layer meander-line polarizer are fabricated and measured as shown in figures 3.18 and 3.19. A 3D printed hollow cylinder is used to stack the polarizer layers on top of the antenna, as shown in figure 3.19 (center picture).

The CP CS-SIW narrow slot antenna using meander-line polarizer as shown in figure 3.17 is simulated using CST software, and the simulated results are compared with measured results. The polarizer distance from the CS-SIW antenna, ph, and the planar dimensions of the polarizer are studied by modifying the parameters.

The radiated fields from the slot (or any other) antenna to free space is spherical waves in nature (see [1], pg. 23). To obtain the plane wave behavior from the radiated spherical waves, we need to locate at a distance, R, far away from the antenna position. The far-field distance, R, should be $> (2D^2)/\lambda_0$ (see [1], eq. 13-16); where D denotes the size of the antenna ($= 2.5\lambda_0$) and λ_0 is the free space wavelength at a given frequency. The value of R should be higher than $5\lambda_0$ (after we substitute the value of D in R equation). Thus, at 30 GHz the value of R (i.e., ph) should be ≥ 50 mm, and the overall CS-SIW slot antenna plus the meander-line polarizer look bulky. Therefore, to reduce the size of the antenna system to have smaller ph value and also achieving acceptable AR, a study on the ph parameter was analyzed using CST software by setting the initial value of $ph = \lambda_0/2$ as shown in figure 3.20. As read from figure 3.20, the axial ratio is too sensitive to ph when spherical waves impinge to the meander-line polarizer. Therefore, only at a discrete distance (such as $ph = 4.02$ mm), the simulated AR is below 2 dB.

The simulated and measured plots for the reflection coefficient, $|S_{11}|$, and realized gain versus frequency (in GHz) for the CP antenna is in acceptable agreement as shown in figure 3.21(a). The frequency range (also known as impedance bandwidth) of the simulated antenna
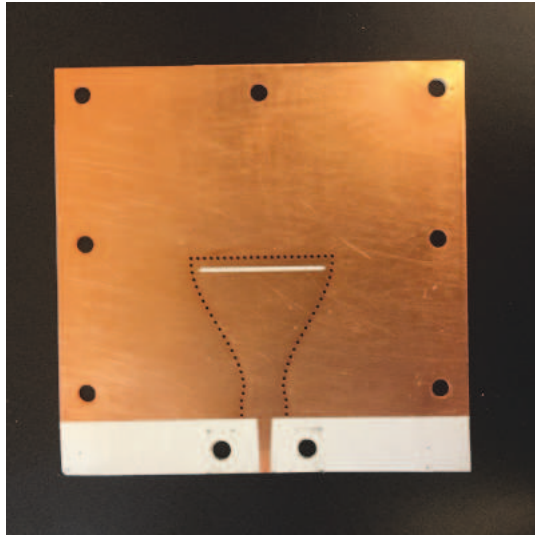
Antenna Layer
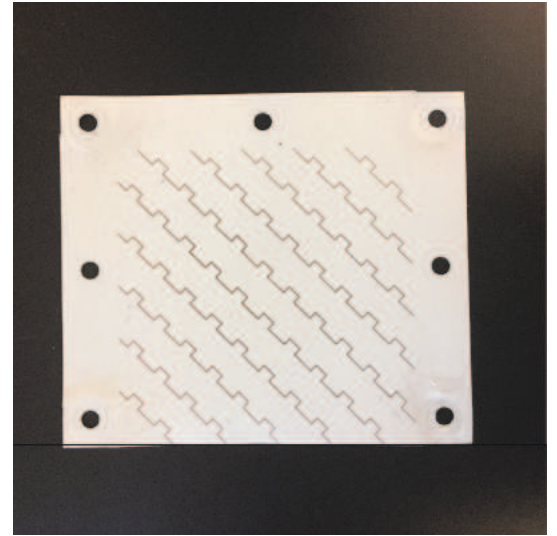
Polarizer Top and Bottom Layer
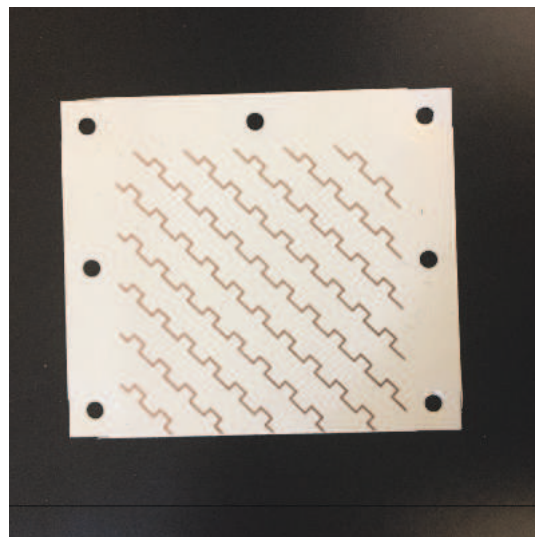
Polarizer Middle Layer

Figure 3.18: Individual layers of the CS-SIW narrow slot antenna using meander-line polarizer.
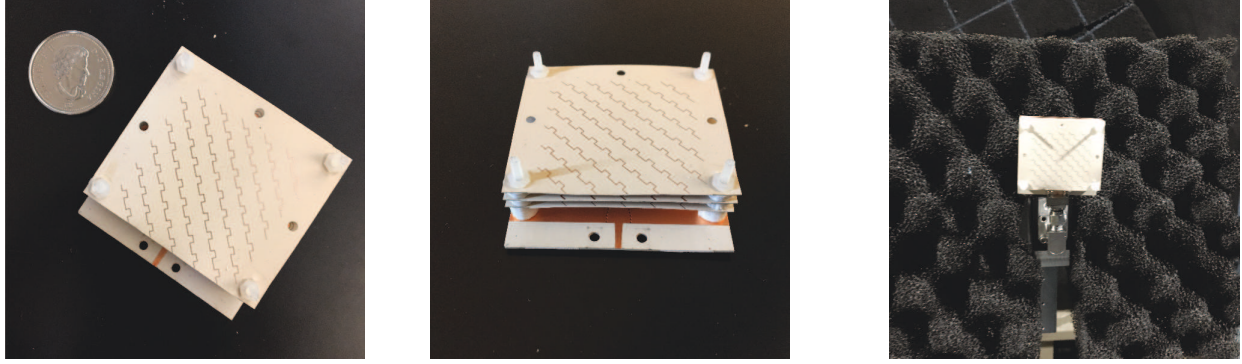
Figure 3.19: (Left) The circularly polarized CS-SIW narrow slot antenna prototype. (Center) front view of the polarizer antenna. (Right) The circularly polarized CS-SIW narrow slot antenna for radiation pattern measurement inside the anechoic chamber.
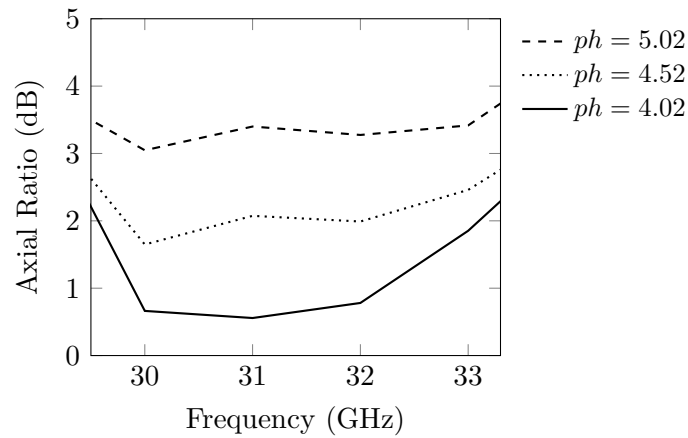
Figure 3.20: Plot of axial ratio (in dB) versus Frequency (in GHz) for different separation height between CS-SIW narrow slot antenna and meander-line polarizer, ph, (in mm).

is from 29.63 - 33.1 GHz and the fractional bandwidth is calculated to be 11.06%. The measured realized gain of a polarizer antenna varies from 7 - 8.96 dB between the impedance bandwidth.

The simulated and measured axial ratio (in dB) versus frequency (in GHz) for the CP antenna is shown in figure 3.21(b), and the simulated and measured axial ratio varies between 0.5 - 2 dB and 2 - 3.5 dB, respectively over the impedance bandwidth. The difference in axial ratio between measured and simulated AR could be due to three reasons: (a) difference in the height of the antenna and polarizer, ph (b) difference in height between the polarizer layers, ps, and (c) unevenness of the thin polarizer sheet. The electric field distribution at 31 GHz and fixed distance, z, for different phases are shown in figure 3.22.
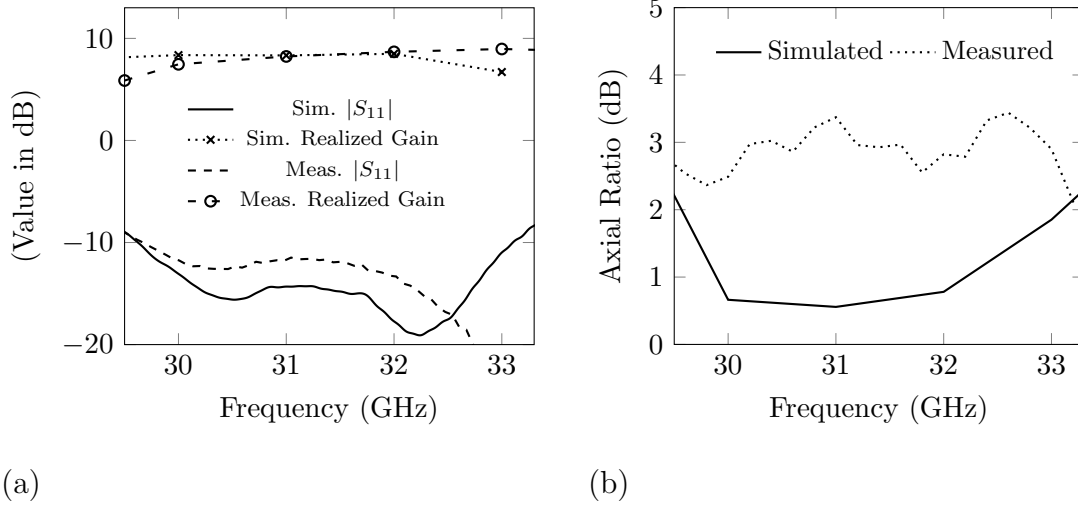
Figure 3.21: CS-SIW narrow slot antenna using meander-line polarizer (a) plot of reflection coefficient, $|S_{11}|$, (in dB) and realized gain (in dB) versus frequency (in GHz); (b) Plot of axial ratio (in dB) versus frequency (in GHz).
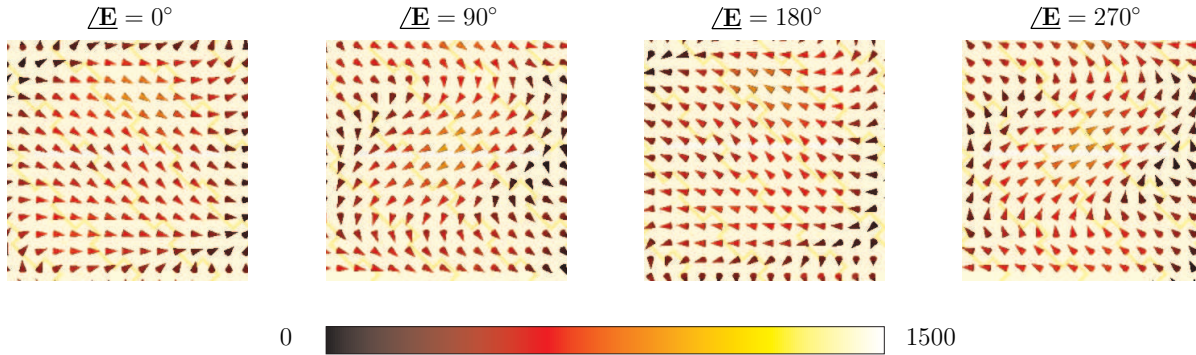
Figure 3.22: Electric field (in V/m) vector plot at 31 GHz (and fixed distance, z).

The normalized E-plane and H-plane radiation pattern at $\phi = 90°$ for the CP CS-SIW narrow slot antenna using meander-line polarizer is shown in figure 3.23 at frequencies 30, 31, 32 and 33 GHz. The measured E-plane radiation pattern is < -20 dB at 90° and 270° for all the frequencies. However, the measured and simulated E-plane radiation pattern is in acceptable range between -45° $\leq \theta \leq$ 45°.

The normalized E-plane and H-plane radiation pattern at $\phi = 90°$ for the CP CS-SIW narrow slot antenna using meander-line polarizer are shown in figure 3.23 at frequencies 30, 31, 32 and 33 GHz. The measured E-plane radiation pattern is < -20 dB at 90° and 270° for all the frequencies. However, the measured and simulated E-plane radiation pattern is in an acceptable range between -45° $\leq \theta \leq$ 45°.

44
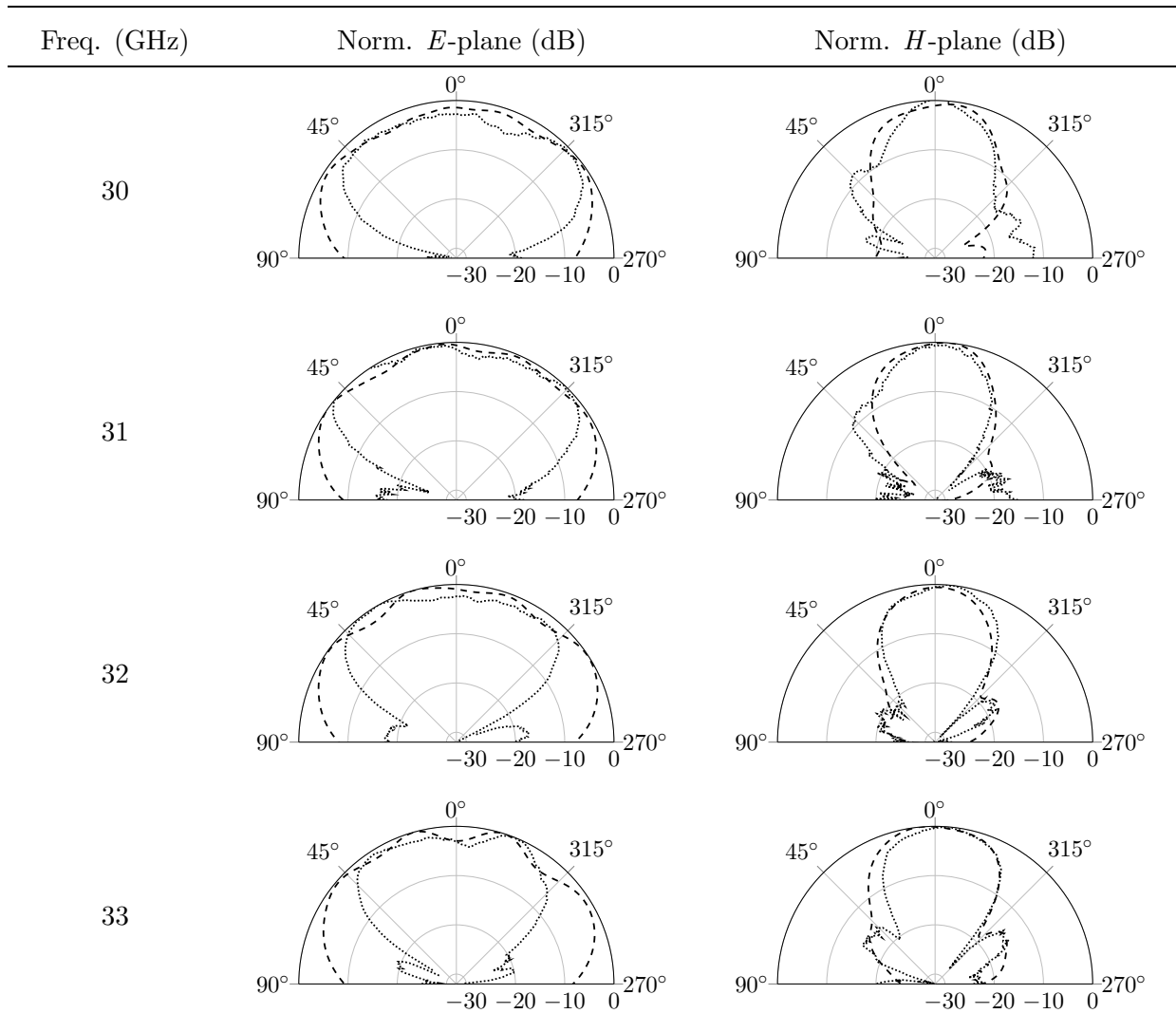
Figure 3.23: Plot of measured (dotted) and simulated (dashed) normalized E-plane and H-plane radiation patterns at $\phi = 90°$ for a CS-SIW slot meander-line polarizer antenna at multiple frequencies.

3.7 Summary

In this chapter, we have proposed a low-profile linearly polarized CS-SIW narrow slot antenna operating at mm-wave frequencies ($\simeq$ 30 GHz). The design methodology for the enhancement of gain and bandwidth is presented. The conventional slot antenna impedance bandwidth ($\simeq$ 3%) can be improved (to >10%) by increasing the length of the slot. Also, the antenna gain can be further enhanced by 2.1 - 2.7 dB to a total gain between 10.5 - 11.44 dB by exciting secondary radiating sources, located at proximity to the primary radiator (i.e.,

slot).

Besides, the two CS-SIW narrow slot antennas were fabricated, measured, and compared with simulation results. The $|S_{11}|$, gain, and principal radiation patterns match with both simulated and measured results. However, the frequency shift of 1.03 GHz is observed between the simulated and measured $|S_{11}|$, which is accounted for the change in dielectric substrate ϵ_r of the fabricated antenna. Moreover, we also saw that we could obtain (ripple free) smooth E-plane radiation pattern with the inclusion of the AMC surface on the top layer of the antenna.

Finally, an LHCP antenna system is designed, simulated, and validated through measurement at mm-wave frequency. The antenna system consists of a CS-SIW narrow slot antenna and a meander-line polarizer. At first, a three-layered meander-line polarizer is designed and simulated using CST software to increase the CP bandwidth in the frequency range 29.63 - 33.1 GHz. Further, to excite the polarizer with EM waves, a linearly polarized CS-SIW narrow slot antenna was preferred. The meander-line polarizer was located on top of the slot antenna at a certain distance. Also, the whole antenna system (i.e., antenna and polarizer) was simulated using CST software. It was observed that the distance between the polarizer and the antenna is too sensitive and can restrict from achieving wide-band axial ratio (AR < 3 dB) across the frequency range 29.63 - 33.1 GHz.

A prototype of the antenna system was fabricated and measured to validate simulated results. The simulated and measured $|S_{11}|$ (in dB) and gain (in dB) versus frequency (in GHz) are in agreement with each other. The impedance bandwidth and the maximum gain are found to be 11.06% and 8.96 dB, respectively. However, measured AR is higher than simulated AR by 1.5 dB across 29.63 - 33.1 GHz. This difference could be due to a change in height between polarizer and antenna, and/or the polarizer layers at mm-wave frequencies.

Chapter 4: The Linear Eight Element LP CS-SIW Narrow Slot Antenna Array

4.1 Introduction

The gain of the single element antenna isn't sufficient to transmit the signal > 0.5 Km in a dense urban environment due to propagation path loss (see [3], sec 3.2). Therefore, we require a high-gain antenna to compensate for the path loss, and also to transmit the signal over long distances. High-gain (or directional) antenna can be achieved by constructing an array of two or more single element antennas and exciting them simultaneously (either with uniform or non-uniform amplitude and phase). The EM fields radiated from each of the single antenna elements in an array is spatially distributed to time, henceforth the area of radiation (technically, the array's physical aperture area) is increased when compared with single standalone antenna physical aperture area. Thus, a high gain can be achieved due to an increase in the array's physical aperture area (see [1], sec.4.4.1). A high gain implies that the antenna beamwidth (evaluated from radiation pattern) is small, and the gain is >15 dB (gain of an horn antenna). The radiation pattern of an antenna array depends on the element-element spacing and the phase of excitation at each antenna element in an array environment and can be studied in-depth as mentioned in (see [1], chap.8; [37], chap.5,6).

In this chapter, we shall design (and simulate), fabricate (and measure) a high gain linear array antenna. The linear array antenna consists eight CS-SIW narrow slot antenna elements which are designed to excite with uniform amplitude and phase.

4.2 Design of 1×8 SIW Power Divider

An effortless method to excite the antenna elements uniformly (with amplitude and phase) in a linear antenna array system is to excite each antenna element in a linear array environment individually. However, by this approach, a large number of resources are consumed (i.e., increase in cost), the overall antenna system looks bulkier and has low practicality. For example, we shall require eight connectors and eight RF signal generators to
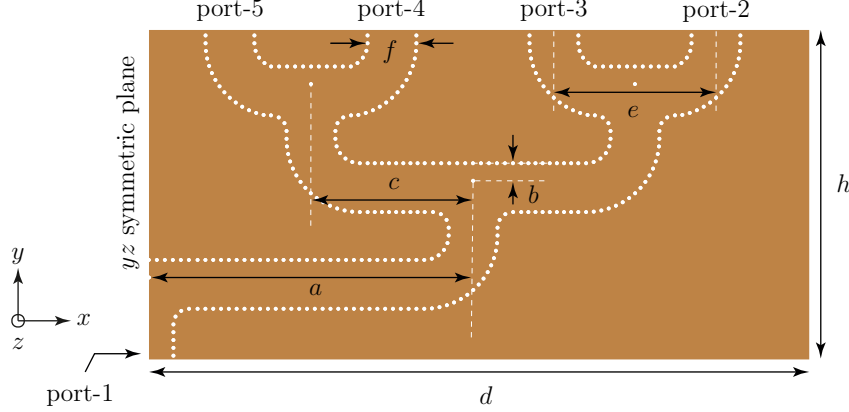
Figure 4.1: Top view of the symmetrical nine port matched SIW power divider and its dimensions (in mm) are $a = 33.174$, $b = 1.8$, $c = 16.6$, $d = 66$, $e = 16.58$, $f = 5$ and $h = 34.377$.

feed the eight element linear array antenna system. Thus, to avoid the complexity, cost and to realize a practical system, it is necessary to design a feeding line where all the ports are matched and also an ability to distribute/divide power equally to all the elements in a linear array system. Hence, the divider is known as an equal split Wilkinson power divider (see [9], sec.7.3). In this thesis, the divider is constructed using SIW technology, and hence, we name the divider as SIW power divider.

The SIW power divider is designed using Rogers 6002 substrate of relative permittivity, $\epsilon_r = 2.94$; loss tangent, $\tan\delta = 0.0012$, and the thickness of the substrate is 0.508 mm (or 20 mils). The SIW power divider is oriented along xy plane, and consists of one input port (port-1) and eight output ports (port-2 to port-9). All the nine ports are matched, and the output ports are aligned linearly at a distance, e, along x axis. Figure 4.1 illustrates only the half top-view of the designed SIW power divider, because the divider is symmetric along yz plane. As observed from figure 4.1, at each T junction a matching post is placed at a distance, b, from the SIW side wall and positioned symmetrical to the center of each T junction. The return loss is minimized with the addition of matching post [38]. The dimensions of the matching post are equal to the dimensions of the via (i.e., length $= 0.508$ mm and diameter $= 0.4$ mm) and are inserted into the Rogers 6002 substrate. The width, f, of the SIW side wall is 5 mm, and the periodicity of the side wall via is 0.8 mm. The overall dimensions of the SIW power divider are $13.2\lambda_0 \times 3.4377\lambda_0 \times 0.0544\lambda_0$ (where λ_0 is the free space wavelength at 30 GHz). The SIW power divider ports are excited by constructing waveguide ports; and the divider was simulated using CST-MS software by exciting port-1 alone. To reduce the computational time by 50%, a PMC boundary condition was applied at the yz symmetric

48
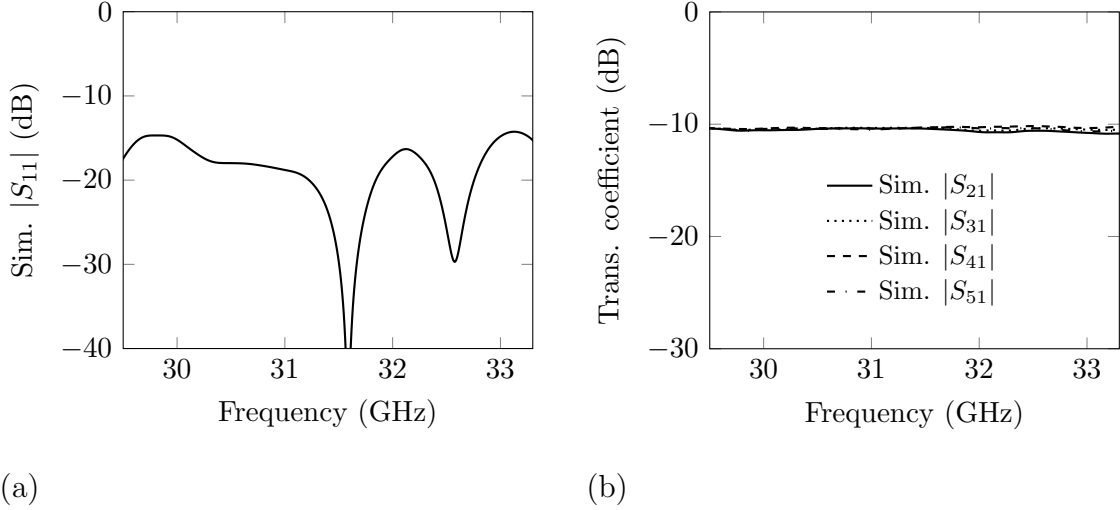
Figure 4.2: Plot of SIW power divider scattering parameters (a) reflection coefficient (in dB) with respect to frequency (in GHz); and (b) transmission coefficients (in dB) with respect to frequency (in GHz).

plane. The plot of simulated scattering parameters with respect to frequency are depicted in figure 4.2. The symmetry nature of the SIW power divider structure enforce four out of eight transmission coefficients to have equal data (i.e., $S_{21} = S_{91}$, $S_{31} = S_{81}$ and so on). Thus, the data plot for the transmission coefficients, S_{21} through S_{51}, versus frequency would only suffice. As read from figure 4.2, the simulated reflection co-efficient, $|S_{11}|$ at port-1 is <-15 dB and the simulated transmission coefficients is around -10.2 dB for the frequency range 29.5 - 33.3 GHz. For an ideal condition, the transmission coefficient should be 9 dB for an eight output 3-dB power divider. The 1.2 dB (= 10.2 - 9) dB increase in insertion loss is accounted for the dielectric and conductor losses.

At first, a 3-port matched SIW power divider was designed and simulated using CST-MS software, to achieve low return loss by varying the parameter for the position of the matching post. Later, a 3-port SIW power divider was extended to design 9-port SIW power divider.

4.3   Design of 1×8 LP CS-SIW Narrow Slot Antenna Array

To realize a linear slot array consisting of eight CS-SIW antenna elements, we now have to combine the designed CS-SIW antenna element (sec.3.2) at each output port of the designed SIW power divider (sec.4.2) and excite the resulting model by using microstrip to SIW transition. The 3D view of the designed linear CS-SIW slot array antenna is shown in figure

49
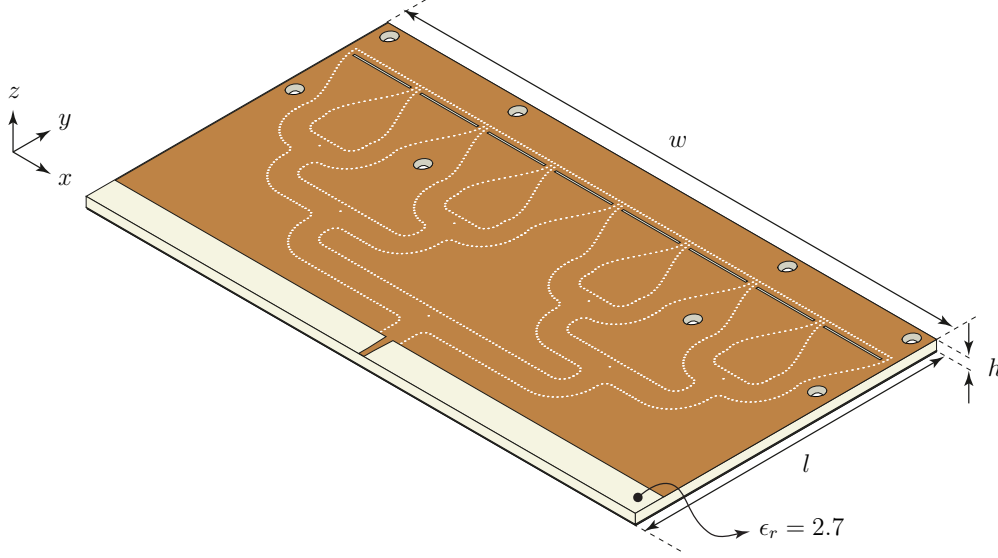
Figure 4.3: 3D view of eight element linear CS-SIW slot array antenna and its corresponding dimensions (in mm) are $l = 64.27$, $w = 135.26$ and $h = 0.544$.

4.3 and is oriented on xy plane. The antenna array is constructed on a layer of Rogers 6002 substrate of relative permittivity, $\epsilon_r = 2.94$; loss tangent, $\tan \delta = 0.0012$, and, the thickness of the substrate and copper trace on both top and bottom sides of the substrate are 0.508 mm (or 20 mils) and 18 μm, respectively. All the antenna elements in an array are excited with the uniform amplitude and phase at each frequency. The overall dimensions of the designed array system is $13.526\lambda_0 \times 6.427\lambda_0 \times 0.0544\lambda_0$ (where λ_0 is the free space wavelength at 30 GHz).

4.4   Results and Discussion

The prototype for the 1×8 CS-SIW narrow slot array antenna was fabricated as shown in figure 4.4, and antenna characteristics such as reflection co-efficient, gain and the radiation pattern were measured.

The array antenna was simulated using CST-MS software by defining a waveguide port to the microstrip line at the origin $((x, y, z) = (0, 0, 0))$. The antenna radiates along $+z$ axis. The plot of simulated and measured reflection coefficient, $|S_{11}|$, (in dB) and realized gain (in dB) with respect to frequency (in GHz) for the proposed eight element linear CS-SIW slot array antenna is shown in figure 4.5(a) and 4.5(b), respectively. As seen from figure

Figure 4.4: (Top) The 1×8 CS-SIW narrow slot antenna array prototype. (Bottom) the 1×8 CS-SIW narrow slot antenna array for radiation pattern measurement inside the anechoic chamber.

Figure 4.5: Plot of simulated and measured eight element linear CS-SIW slot array antenna for (a) reflection coefficient, $|S_{11}|$, (in dB) versus Frequency (in GHz); and (b) realized gain (in dB) versus Frequency (in GHz).
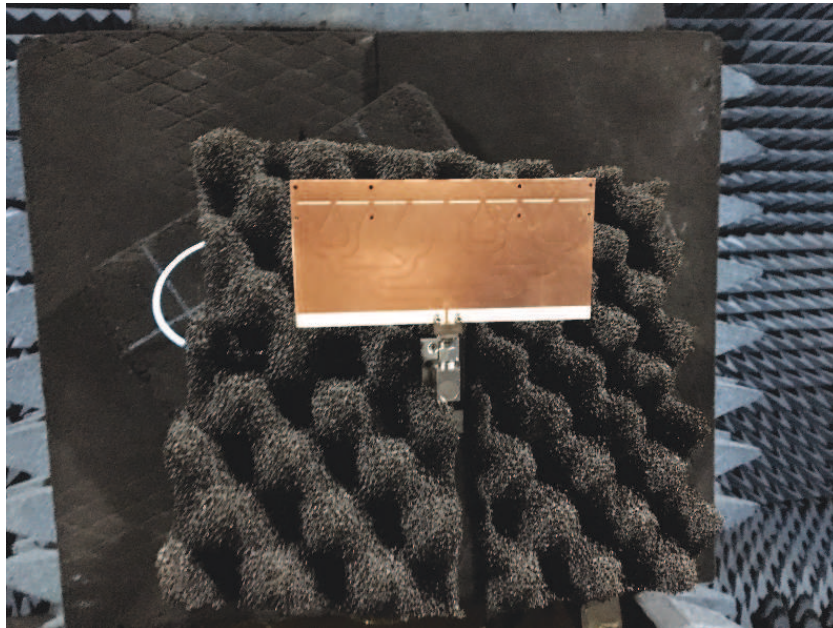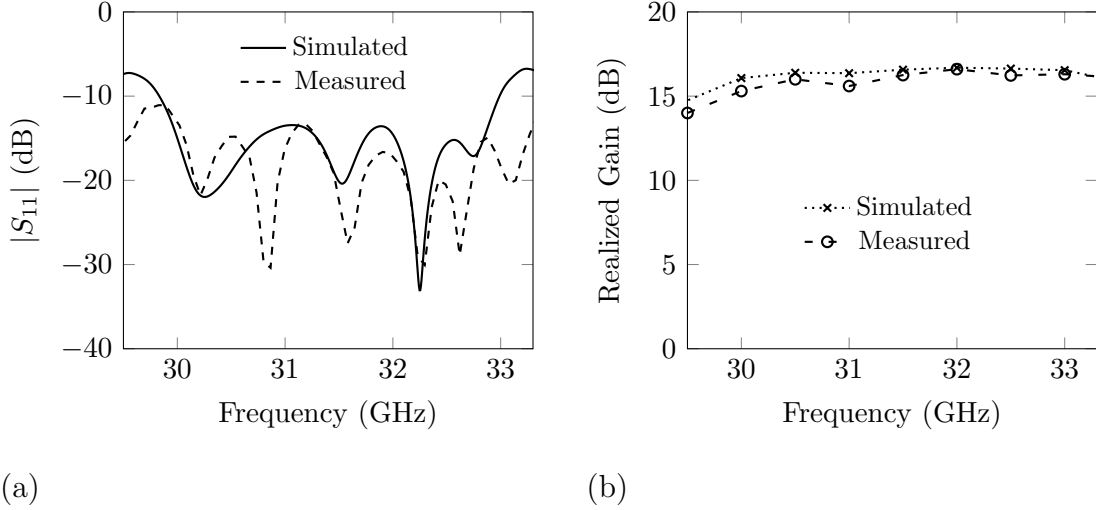
4.5(a), the simulated and measured reflection coefficient, $|S_{11}|$, plots are matching with each other and the $|S_{11}|$ is < -10 dB in the frequency range from 29.8 to 33 GHz. The calculated fractional bandwidth is found to be 10.2%. As read from figure 4.5(b), the maximum and minimum measured realized gain occurs at 32 GHz and 30 GHz, and are equal to 16.6 dB and 15.3 dB, respectively. In addition, the plot of simulated realized gain matches with the plot of measured realized gain for the CS-SIW slot array antenna. An average increase in the realized gain of $\simeq$ 7.3 dB (out of 9 dB for an ideal case) is observed across the frequency matching bandwidth, by designing eight-element linear array antenna than the standalone CS-SIW antenna as shown in figure 4.6(a). The decrease in the gain of 1.7 dB is equal to the summation of leakage losses, imperfect material losses, and mismatch losses in the feeding network. The leakage losses are negligible, and hence they are neglected. The imperfect material losses such as dielectric and conductor losses are about 0.0116 dB/mm, which accumulates to $\simeq$ 1.1 dB of loss for the whole feeding network. The mismatch losses are about 0.5 dB. The mismatch losses are observed at the T-junction due to the placement of matching via. The transition loss between the microstrip line and SIW is 0.1 dB.

The normalized, simulated and measured principal plane radiation patterns for an eight element linear CS-SIW slot array antenna are shown in figure 4.7. The array antenna E-plane pattern is along the yz plane (i.e., $\phi = 90°$ and $0° \leq \theta \leq 180°$) and H-plane pattern is along the xz plane (i.e., $\phi = 0°$ and $0° \leq \theta \leq 180°$). The normalized radiation patterns are plotted at multiple frequencies starting from 30 GHz, in step size of 1 GHz. Since, the measured

52
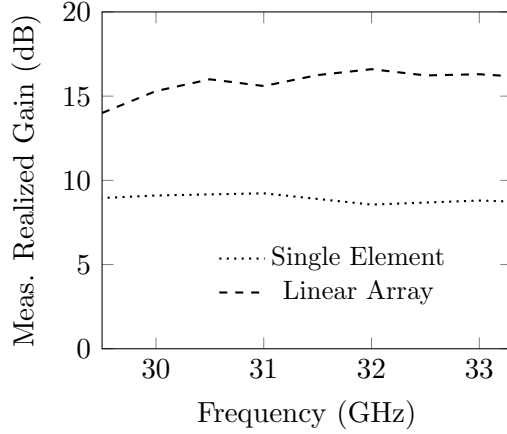
Figure 4.6: Comparison plot of measured realized gain (in dB) between CS-SIW single element and eight-element linear CS-SIW slot array antenna versus frequency (in GHz).

principal plane radiation pattern varies only from $-90° \leq \theta \leq 90°$, all the simulated principal plane radiation patterns in figure 4.7 are limited to $-90° \leq \theta \leq 90°$, which help us to have meaningful comparison at specific (x,y) points. The half-power beamwidth is different for both E-plane and H-plane, due to the linear alignment of the CS-SIW antenna elements in an array. The measured E-plane radiation pattern at each frequency plot in figure 4.7 is similar to the simulated E-plane pattern. The simulated and measured H-plane radiation pattern at each frequency plot as shown in figure 4.7 has side-lobe level (SLL) greater than -10 dB. The high SLL, is due to the wide spacing of $1.658\lambda_0$ (where λ_0 is the free space wavelength at 30 GHz) between the CS-SIW slot antenna elements in a linear array.

4.5   Design of 1×8 LP CS-SIW Narrow Slot Antenna Array with Superstrate

For any given antenna, the presence of side lobe level (SLL) (which is comparable to main lobe level) in the antenna radiation pattern deteriorates its performance. For instance, the SLL causes unwanted radiation at undesired locations which may have interference with the antenna main lobe. Therefore, to reduce the SLL, two methods are presented; namely 'dielectric slab cover' and 'extended horn groove' [39]. In this thesis, the gain of an antenna (main lobe) is further increased by using a superstrate on top of the 1×8 slot radiator's at height, h [40].
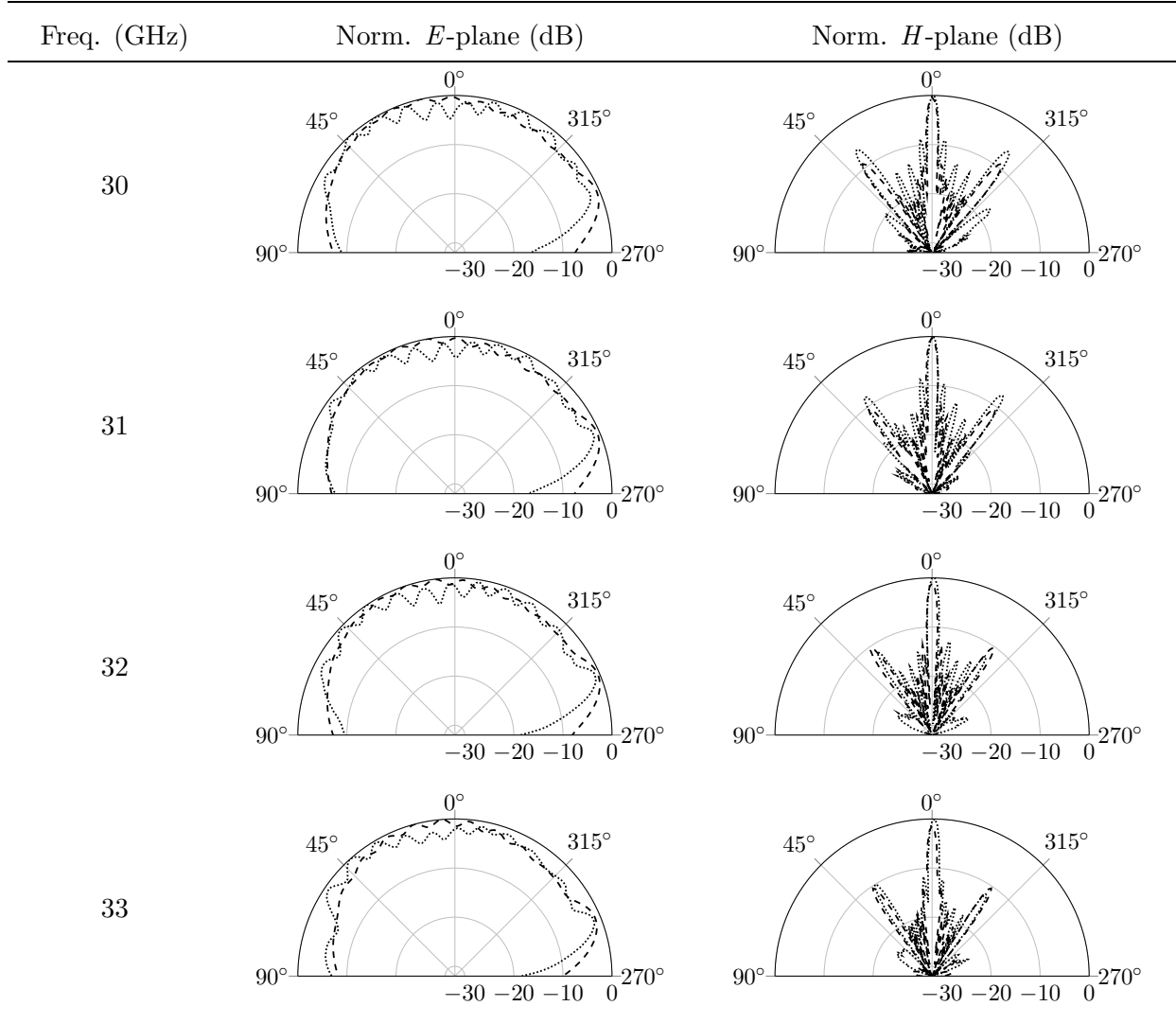
Figure 4.7: Measured (dotted) and simulated (dashed) normalized radiation patterns (E-plane ($\phi = 90°$) and H-plane ($\phi = 0°$)) for an eight-element linear CS-SIW slot array antenna at multiple frequencies.

The 3D model of the designed antenna to reduce the SLL is shown in figure 4.8. The designed antenna model consists of an eight-element CS-SIW linear slot array antenna (as discussed in sec.4.3) and a superstrate. The plane of the superstrate is parallel to the plane of the array antenna, and the superstrate is placed on top of the linear array radiating elements at a distance, $h = 5.4$ mm ($\simeq \lambda_0/2$ where λ_0 is the free space wavelength at 30 GHz). Rogers RO3010 material is preferred as a superstrate in our designed model owing to its high relative permittivity, $\epsilon_r = 10.2 \pm 0.3$ at 10 GHz, and loss tangent, $\tan\delta = 0.0022$. The thickness of the superstrate, st, is equal to 0.64 mm ($\simeq \lambda_g/4$ where λ_g is the guided wavelength inside the superstrate at 30 GHz).

Figure 4.8: 3D view of eight-element linear CS-SIW slot array antenna with superstrate and its corresponding dimensions (in mm) are $sl = 135.26$, $sw = 17.2$, $h = 5.4$, $st = 0.64$ and $l = 64.27$.

4.6   Results and Discussion

The antenna model and the fabricated prototype of the antenna are shown in figures 4.8 and 4.9, respectively. Also, the model is simulated using CST-MS software by designing a waveguide port for the microstrip line at the origin. The distance between the superstrate and the array antenna for the fabricated prototype is ensured by 3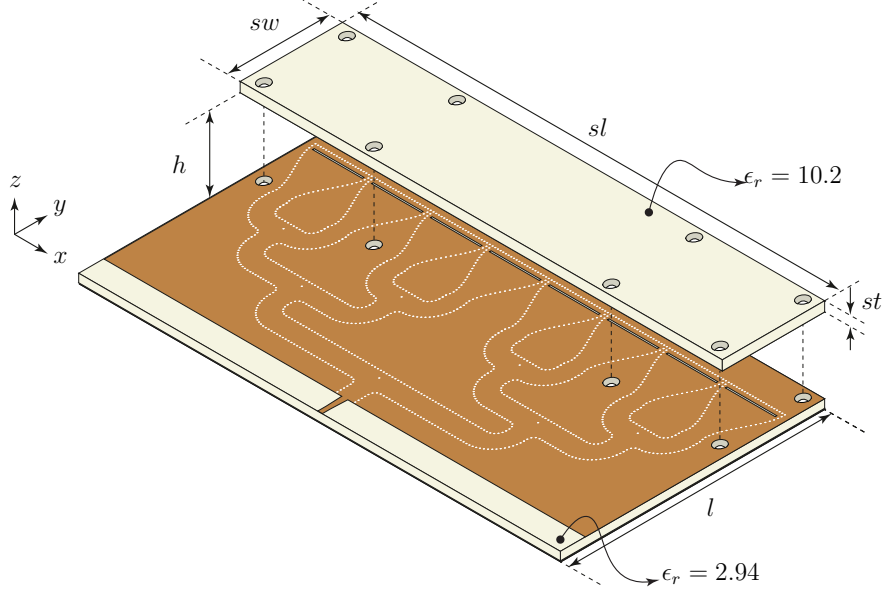D printing hollow cylindrical spacer of height, h, and the dimensions for the inner and outer diameters are 3 mm and 6 mm, respectively. The reflection coefficient, $|S_{11}|$, gain, and the normalized principal plane radiation patterns for the fabricated prototype are measured, and these results are shown in figure 4.10 and 4.11, respectively.

The frequency range of the measured impedance bandwidth is from 30 - 33.14 GHz as seen from figure 4.10(a) and the fractional bandwidth is calculated to be 9.95%. The measured and simulated impedance bandwidths are matched (as shown in figure 4.10(a)). The reflection coefficient, realized gain and the normalized principle plane radiation patterns for the simulated antenna model (figure 4.8) are plotted in figures 4.10, 4.11, respectively. The measured and simulated realized gain are similar with each other as shown in figure 4.10(b). The measured realized gain varies from 18.66 - 21.44 dB and the maximum gain is observed at 32 GHz; while, the simulated realized gain varies from 21.35 - 22.95 dB and the
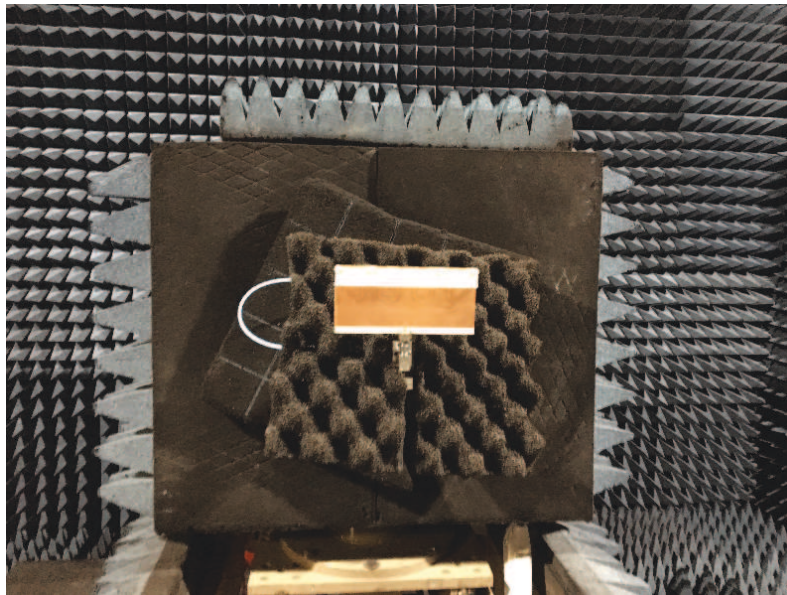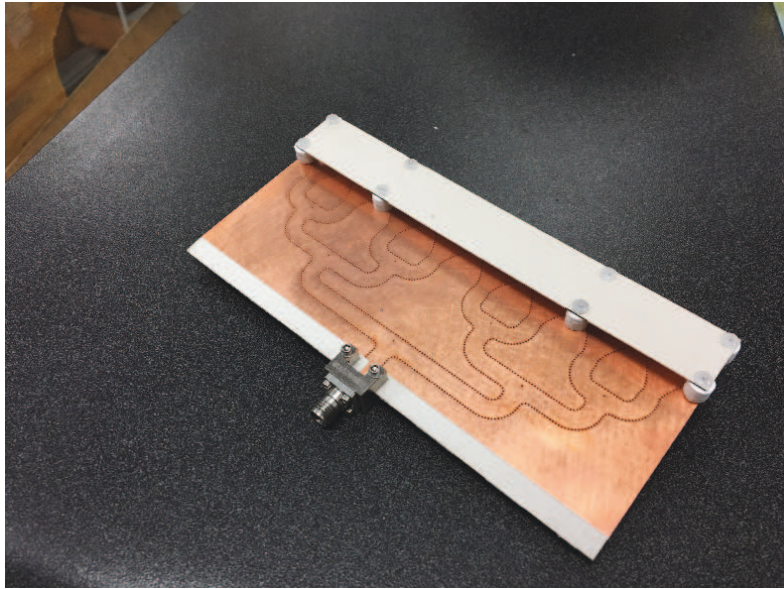
Figure 4.9: (Top) The 1×8 CS-SIW narrow slot antenna array prototype with superstrate. (Bottom) The 1×8 CS-SIW narrow slot antenna array with superstrate for radiation pattern measurement inside the anechoic chamber.
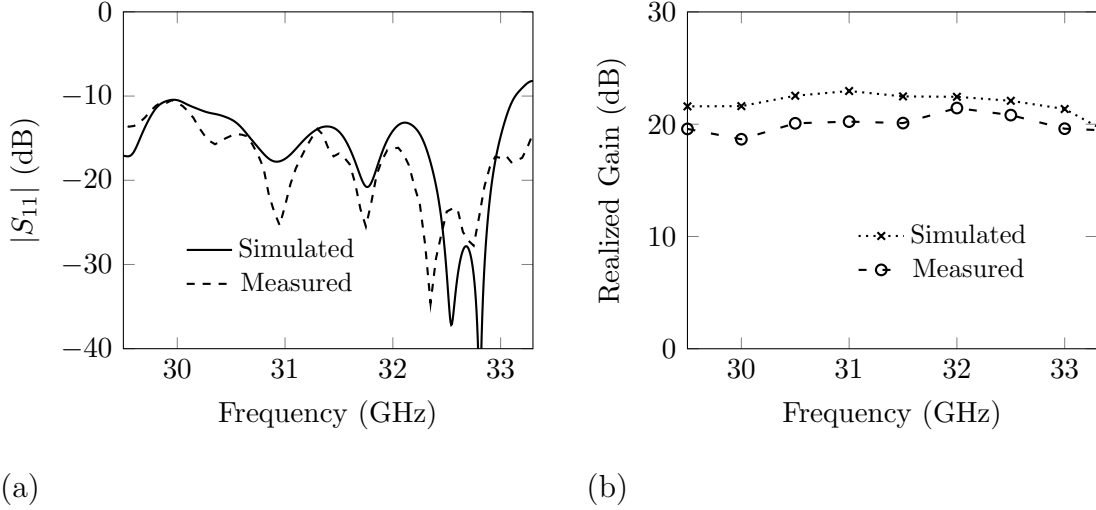
Figure 4.10: Measured and simulated plots for eight-element linear CS-SIW slot array antenna with superstrate (a) reflection coefficient, $|S_{11}|$, (in dB) versus frequency (in GHz); and (b) realized gain (in dB) versus frequency (in GHz).

maximum gain is observed at 31 GHz. Thus, the gain increases by 6 dB with the addition of the superstrate.

Furthermore, the normalized E-plane radiation pattern is comparable to both measured and simulated plots at respective frequencies. However, the ripples are observed in the measured E-plane normalized pattern at 31 - 33 GHz due to diffraction (see [1], pp.730) and also possibly, due to induced current on the volume of the metallic southwest connector. The normalized measured H-plane has multiple side lobes and is higher in magnitude across the impedance bandwidth of an antenna with superstrate. The reason could be the critical distance between the array radiating elements and the superstrate. Besides, the inclusion of spacers between the superstrate and ground plane may impact the radiation pattern, because, the material used to fabricate spacers might have relative permittivity, which is not equal to one. The simulated H-plane SLL is further improved by -10.03, -8.37, -8.80 and 4.47 dB at frequencies 30, 31, 32 and 33 GHz, respectively with the addition of superstrate. Thus, the simulated H-plane SLL level is < -14 dB for the overall impedance bandwidth. The measured and simulated gain and H-plane SLL plot versus frequency are compared, as shown in figure 4.12 for the CS-SIW array models with and without superstrate.
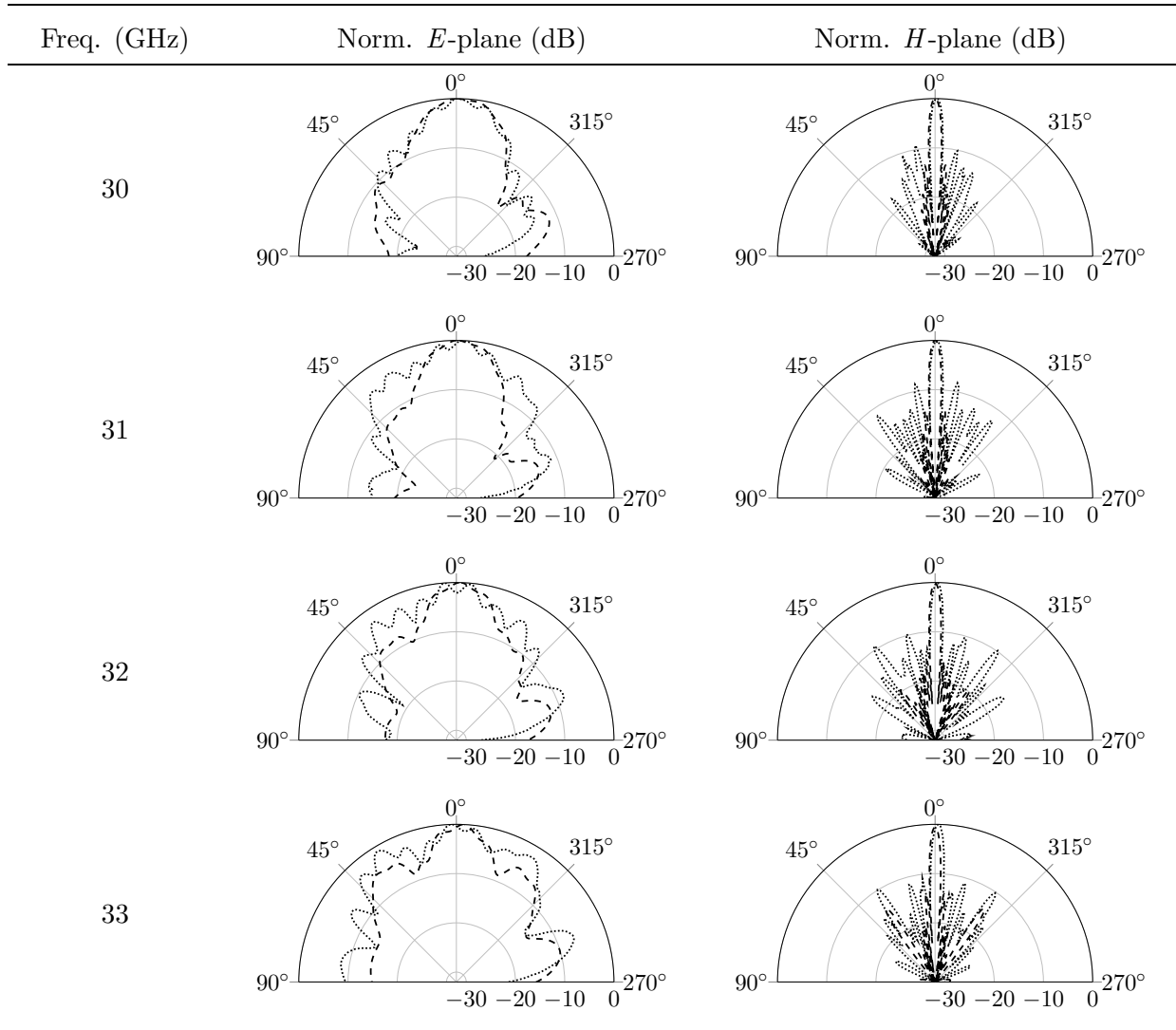
Figure 4.11: Measured (dotted) and simulated (dashed) normalized radiation patterns (E-plane ($\phi = 90°$) and H-plane ($\phi = 0°$)) for an eight-element linear CS-SIW slot array antenna with superstrate at multiple frequencies.

4.7 Summary

In this chapter, a high-gain antenna is realized by designing a linear array of eight CS-SIW narrow slot elements, at mm-wave frequency ($\simeq 30$ GHz). High SLL are observed for the linear array due to $> \lambda_g$ spacing between the antenna elements.

A superstrate with a high dielectric constant on top of the radiating slot's in a linear array increases the gain of the antenna by 6 dB and therefore, decrease SLL. The simulation and
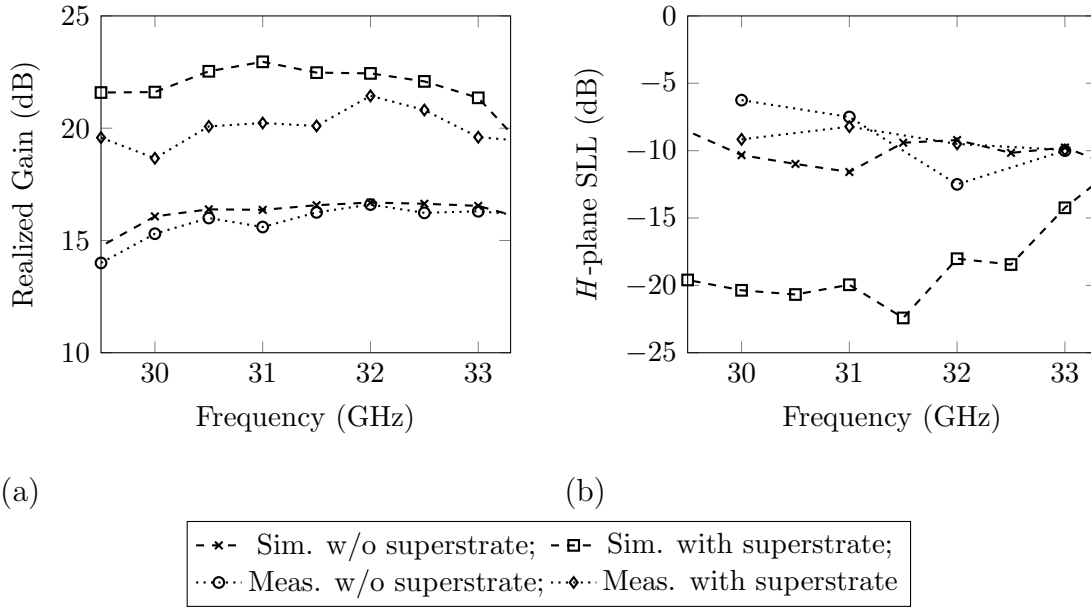
Figure 4.12: Measured and simulated comparison plots between eight-element linear CS-SIW slot array antenna with and without superstrate (a) realized gain (in dB) versus frequency (in GHz); and (b) H-plane SLL (in dB) versus frequency (in GHz).

measurement results are presented and compared for both, linear CS-SIW narrow slot array antenna with and without superstrate. The impedance bandwidth for both array antennas are around 10%. The maximum measured gain for the array antenna with and without superstrate are 21.44 dB and 16.6 dB, respectively at 32 GHz.

Chapter 5: Conclusion

In this work, we have proposed and presented an LP and CP antennas using SIW at mm-wave frequencies ($\simeq$ 30 GHz). The antennas were fabricated using a low-cost material and are planar — suitable to integrate with RF back-end circuits. SIW guiding structures were preferred over microstrip or CPW to minimize the radiation losses at mm-wave frequencies. An LP antenna array was designed to achieve high-gain to compensate for the known propagation path loss at mm-wave frequencies. Therefore, the proposed potential antennas can be used to serve cellular wireless communication networks at mm-wave frequencies.

An LP slot antenna element is designed based on cylindrical sector substrate integrated waveguide (CS-SIW) at f_c=30 GHz. The antenna was modeled and simulated using CST-MS software. Also, it was fabricated and measured using a VNA and anechoic chamber. By increasing the slot length, antenna impedance bandwidth improved to >10% (29.72 to 33 GHz). The simulated and measured realized gain of the antenna is found to be 8.33 - 8.84 dB and 8.56 - 9.1 dB, respectively. Further, to increase the gain of the CS-SIW antenna element, an ungrounded dielectric layer ungrounded on both sides consisting of EBG cells and parasitic patches are constructed on top of the slot. The gain of the modified CS-SIW antenna with the top layer resulted in a 2.1 - 2.7 dB increase when compared with a single-layer CS-SIW slot antenna. The comparison between the simulated and measured results are shown and are in acceptable level for the reflection coefficient, realized gain, and principal plane radiation patterns.

A three-layered meander-line polarizer was designed, simulated, fabricated, and measured at f_c=30 GHz. The polarizer's significance is - to transform the linearly polarized waves into circularly polarized waves. The impedance bandwidth of the CS-SIW slot antenna along with polarizer is found to be >10% (29.63 - 33.1 GHz). Also, the maximum measured gain is found to be 8.96 dB at 33 GHz. The simulated AR is in between 0.5 - 2 dB over the bandwidth. However, the measured AR vary from 2 - 3.5 dB. The change in AR could be due to the delicate spacing between the antenna and polarizer, and also between polarizer layers at mm-wave frequencies. The measured and simulated radiation patterns at $\phi = 90°$ are presented at multiple frequencies and are in acceptable level.

A 1×8 CS-SIW slot antenna array is proposed at f_c=30 GHz. The linear array antenna was excited with uniform amplitude and phase by designing a 1×8 power divider network using SIW. The insertion loss is found to be ≃10.2 dB across the 8 output ports of the power divider. Therefore, it is estimated that the dielectric losses and the conductor losses of the 1×8 SiW power divider are found to be 1.2 dB. The measured impedance bandwidth and measured peak gain of the 1×8 CS-SIW slot antenna array are ≃10% and 16.6 dB, respectively. However, high SLL is observed in the principal plane radiation pattern of the antenna array due to wide spacing ($> \lambda_0$) between the antenna array elements. Therefore, to decrease high SLL, a superstrate is constructed on top of the 1×8 CS-SIW slot antenna array. As a result, the SLL is < -15 dB across the bandwidth for the simulated antenna, which is an increase of 6 dB when compared to the standalone antenna array. The measured gain and SLL are not in agreement with the simulated results due to the distance between the antenna array and the superstrate. The maximum measured gain for the 1×8 CS-SIW slot antenna array with superstrate is found to be 21.44 dB at 32 GHz.

5.1   Future Work

The designed antenna models, as shown in this thesis, are suitable for applications such as point to point (P2P) wireless communications at mm-wave frequencies. Few suggestions and recommendations for future work include:

1 Antenna performance deteriorates when the distance between the antenna and super-strate or the meander-line polarizer is changed to a small degree (as described in chapter 3 and 4), especially at mm-wave frequencies. In addition, these antenna structures are bulky in nature. One solution to address the aforementioned issues, to investigate and design an engineered surface which is not bulkier (in the case of polarizer) and can be placed on top of the CS-SIW slot antenna at precise and reduced distance.

2 The analytical study on the AR results when the distance between the CS-SIW slot antenna and the meander-line polarizer is less than $\lambda_0/2$.

3 To design an engineered layer on top of the CS-SIW array antenna which can achieve (a) beam tilt (b) beam shape or split.

Bibliography

[1] W. L. Stutzman and G. A. Thiele, *Antenna Theory and Design*. John Wiley & Sons, 2012.

[2] J. L. Volakis, *Antenna Engineering Handbook*. McGraw-Hill, 2007.

[3] T. S. Rappaport, R. W. Heath Jr, R. C. Daniels, and J. N. Murdock, *Millimeter Wave Wireless Communications*. Pearson Education, 2014.

[4] T. S. Rappaport, S. Sun, R. Mayzus, H. Zhao, Y. Azar, K. Wang, G. N. Wong, J. K. Schulz, M. Samimi, and F. Gutierrez, "Millimeter wave mobile communications for 5g cellular: It will work!" *IEEE Access*, vol. 1, pp. 335–349, 2013.

[5] S. Rangan, T. S. Rappaport, and E. Erkip, "Millimeter wave cellular wireless networks: Potentials and challenges," *Proceedings of the IEEE*, vol. 102, no. 3, pp. 366–385, 2014.

[6] C. A. Balanis, *Antenna Theory: Analysis and Design*. John Wiley & sons, 2016.

[7] R. Paknys, *Applied Frequency-Domain Electromagnetics*. Wiley/IEEE Press, 2016.

[8] H. G. Booker, "Slot aerials and their relation to complementary wire aerials (babinet's principle)," *Journal of the Institution of Electrical Engineers-Part IIIA: Radiolocation*, vol. 93, no. 4, pp. 620–626, 1946.

[9] D. M. Pozar, *Microwave Engineering*. John Wiley & Sons, 2012.

[10] M. Bozzi, A. Georgiadis, and K. Wu, "Review of substrate-integrated waveguide circuits and antennas," *IET Microwaves, Antennas & Propagation*, vol. 5, no. 8, pp. 909–920, 2011.

[11] F. Xu and K. Wu, "Guided-wave and leakage characteristics of substrate integrated waveguide," *IEEE Transactions on Microwave Theory and Techniques*, vol. 53, no. 1, pp. 66–73, 2005.

[12] G. Q. Luo, Z. F. Hu, L. X. Dong, and L. L. Sun, "Planar slot antenna backed by substrate integrated waveguide cavity," *IEEE Antennas Wireless Propag. Lett*, vol. 7, no. 1, pp. 236–239, 2008.

[13] S. Mukherjee, A. Biswas, and K. V. Srivastava, "Broadband substrate integrated waveguide cavity-backed bow-tie slot antenna," *IEEE Antennas and Wireless Propagation Letters*, vol. 13, pp. 1152–1155, 2014.

[14] M. Li and K.-M. Luk, "Low-cost wideband microstrip antenna array for 60-ghz applications," *IEEE Transactions on Antennas and Propagation*, vol. 62, no. 6, pp. 3012–3018, 2014.

[15] K. Gong, Z. N. Chen, X. Qing, P. Chen, and W. Hong, "Substrate integrated waveguide cavity-backed wide slot antenna for 60-ghz bands," *IEEE Transactions on Antennas and Propagation*, vol. 60, no. 12, pp. 6023–6026, 2012.

[16] X.-P. Chen, K. Wu, L. Han, and F. He, "Low-cost high gain planar antenna array for 60-ghz band applications," *IEEE Transactions on Antennas and Propagation*, vol. 58, no. 6, pp. 2126–2129, 2010.

[17] G. Q. Luo, Z. F. Hu, Y. Liang, L. Y. Yu, and L. L. Sun, "Development of low profile cavity backed crossed slot antennas for planar integration," *IEEE Transactions on Antennas and Propagation*, vol. 57, no. 10, pp. 2972–2979, 2009.

[18] Y. Lang, S.-W. Qu, and J.-X. Chen, "Wideband circularly polarized substrate integrated cavity-backed antenna array," *IEEE Antennas and Wireless Propagation Letters*, vol. 13, pp. 1513–1516, 2014.

[19] A. B. Guntupalli and K. Wu, "60-ghz circularly polarized antenna array made in low-cost fabrication process," *IEEE Antennas and Wireless Propagation Letters*, vol. 13, pp. 864–867, 2014.

[20] "Computer simulation technology microwave studio (electromagnetic field simulation software)," https://www.cst.com/products/cstmws, version 2017.

[21] N. Marcuvitz, *Waveguide Handbook*, 1986.

[22] R. F. Harrington, *Time-Harmonic Electromagnetic Fields.* Wiley-IEEE Press, 2001.

[23] P.-S. Kildal, "Definition of artificially soft and hard surfaces for electromagnetic waves," *Electronics Letters*, vol. 24, no. 3, pp. 168–170, 1988.

[24] Y. Al-Alem and A. A. Kishk, "Millimeter wave high gain printed monopole antenna," *Int.'l Symp. on Antenna Technol. and Applied Electromag.*, pp. 1–3, 2018.

[25] ——, "High gain 60 ghz slot antenna with symmetric radiation characteristics," *IEEE Transactions on Antennas and Propagation*, 2019.

[26] D. Sievenpiper, L. Zhang, R. F. Broas, N. G. Alexopolous, E. Yablonovitch *et al.*, "High-impedance electromagnetic surfaces with a forbidden frequency band," *IEEE Transactions on Microwave Theory and Techniques*, vol. 47, no. 11, pp. 2059–2074, 1999.

[27] H. Jin, W. Che, K.-S. Chin, W. Yang, and Q. Xue, "Millimeter-wave te 20-mode siw dual-slot-fed patch antenna array with a compact differential feeding network," *IEEE Transactions on Antennas and Propagation*, vol. 66, no. 1, pp. 456–461, 2017.

[28] T. Y. Yang, W. Hong, and Y. Zhang, "Wideband millimeter-wave substrate integrated waveguide cavity-backed rectangular patch antenna," *IEEE Antennas and Wireless Propagation Letters*, vol. 13, pp. 205–208, 2014.

[29] H. Sun, Y.-X. Guo, and Z. Wang, "60-ghz circularly polarized u-slot patch antenna array on ltcc," *IEEE Transactions on Antennas and Propagation*, vol. 61, no. 1, pp. 430–435, 2012.

[30] J.-S. Park, J.-B. Ko, H.-K. Kwon, B.-S. Kang, B. Park, and D. Kim, "A tilted combined beam antenna for 5g communications using a 28-ghz band," *IEEE Antennas and Wireless Propagation Letters*, vol. 15, pp. 1685–1688, 2016.

[31] S. Alkaraki, A. S. Andy, Y. Gao, K.-F. Tong, Z. Ying, R. Donnan, and C. Parini, "Compact and low-cost 3-d printed antennas metalized using spray-coating technology for 5g mm-wave communication systems," *IEEE Antennas and Wireless Propagation Letters*, vol. 17, no. 11, pp. 2051–2055, 2018.

[32] S. S. Gao, Q. Luo, and F. Zhu, *Circularly Polarized Antennas*.   John Wiley & Sons, 2013.

[33] L. Young, L. Robinson, and C. Hacking, "Meander-line polarizer," *IEEE Transactions on Antennas and Propagation*, vol. 21, no. 3, pp. 376–378, 1973.

[34] M.-A. Joyal and J.-J. Laurin, "Analysis and design of thin circular polarizers based on meander lines," *IEEE Transactions on Antennas and Propagation*, vol. 60, no. 6, pp. 3007–3011, 2012.

[35] C. Terret, J. Levrel, and K. Mahdjoubi, "Susceptance computation of a meander-line polarizer layer," *IEEE Transactions on Antennas and Propagation*, vol. 32, no. 9, pp. 1007–1011, 1984.

[36] B. A. Munk, *Finite Antenna Arrays and FSS.* John Wiley & Sons, 2003.

[37] R. E. Collin and F. J. Zucker, "Antenna theory," 1969.

[38] S. Germain, D. Deslandes, and K. Wu, "Development of substrate integrated waveguide power dividers," in *CCECE 2003-Canadian Conference on Electrical and Computer Engineering. (Cat. No. 03CH37436)*, vol. 3, 2003, pp. 1921–1924.

[39] M. Al Sharkawy and A. A. Kishk, "Long slots array antenna based on ridge gap waveguide technology," *IEEE Transactions on Antennas and Propagation*, vol. 62, no. 10, pp. 5399–5403, 2014.

[40] D. Jackson and N. Alexopoulos, "Gain enhancement methods for printed circuit antennas," *IEEE Transactions on Antennas and Propagation*, vol. 33, no. 9, pp. 976–987, 1985.